Assessing Typhoon Soulik-induced morphodynamics over the Mokpo coast region in South Korea based on a geospatial approach

Sang-Guk Yum[1], Moon-Soo Song[2], Manik Das Adhikari[3*]

[1] Department of Civil Engineering, Gangneung-Wonju National University, Gangneung, Gangwon-do 25457, South Korea; skyeom0401@gwnu.ac.kr
[2] Department of Safety & Disaster Prevention Engineering, Kyungwoon University, Gumi, Gyeongsangbuk-do 39160, South Korea; songms0722@ikw.ac.kr
[3] Department of Civil Engineering, Gangneung-Wonju National University, Gangneung, Gangwon-do 25457, South Korea; rsgis.manik@gmail.com

Correspondence to: Manik Das Adhikari (rsgis.manik@gmail.com)

Abstract

The inner shelf and coastal region of the Yellow Sea along the Korean peninsula are frequently impacted by Typhoons. The Mokpo coastal region in South Korea was significantly affected by typhoon Soulik in 2018, the deadliest typhoon strike to the southwestern coast since Maemi in 2003. Typhoon Soulik overran the region, causing extensive damage to the coast, shoreline, vegetation, and coastal geomorphology. Therefore, it is important to investigate its impact on the coastal ecology, landform, erosion/accretion, suspended sediment concentration (SSC) and associated coastal changes along the Mokpo region.

In this study, net shoreline movement (NSM), ~~Normalized Difference Vegetation Index~~normalized difference vegetation index (NDVI~~)),~~), fractional vegetation coverage (FVC), coastal landform change model, ~~Normalized Difference Suspended Sediment Index~~normalized difference suspended sediment index (NDSSI), and SSC-reflectance relation have been used to analyze the coastal morphodynamics over the typhoon periods. We used pre-and post-typhoon Sentinel-2B MSI images for mapping and monitoring the typhoon effect. The findings highlighted the significant impacts of typhoons on coastal dynamics, wetland vegetation and sediment resuspension along the Mokpo coast. It has been observed that typhoon-induced SSC influences shoreline and coastal morphology. The outcome of this research may provide databases to manage coastal environments and a long-term plan to restore valuable coastal habitats. In addition, the findings may be useful for post-typhoon emergency response, coastal planners, and administrators involved in the long-term development of human life.

Keywords: Typhoon Soulik, Coastal changes, NDVI, FVC, Suspended sediment movement, Shoreline change, Mokpo Coast.

1. Introduction

Typhoons are one of the most destructive natural calamities. Strong winds that accompany typhoons during landfall damage the environment, coastline, wildlife, people, and public and private properties in coastal and inland areas (Shamsuzzoha et al., 2021; Xu et al., 2021; Mishra et al., 2021a; Nandi et al., 2020; Sadik et al., 2020; Sahoo and Bhaskaran, 2018; Hoque et al., 2016). Many coastal and near-coastal countries are plagued by typhoon-induced storms, flooding, deforestation, and increased soil salinity (Rodgers et al., 2009). Typhoons (tropical cyclones) have caused 1,942 disasters in the past 50 years, resulting in 779,324 fatalities and USD 1,407.6 billion in economic losses worldwide (WMO, 2020), demonstrating their effects on both the global and regional economies (Bhuiyan and Dutta, 2012; Mallick et al., 2017). The effects of typhoons include saltwater intrusion, soil fertility depletion, reduced agricultural productivity, life losses, coastline erosion, vegetation damage, and massive economic disasters (Mishra et al., 2021b).

According to instrumental data collected since 1904, typhoon intensity on the Korean peninsula has grown during the previous 100 years (Yu et al., 2018; Cha et al., 2021). A total of 188 typhoons, about three annually, have affected the coastal region from 1959 to 2018 (KMA, 2018). Among past Typhoons, RUSA (2002), MAEMI (2003), NARI (2007), and SOULIK (2018) heavily affected the southwestern coast, causing extensive damage to lives and properties (KMA, 2011; 2018). Furthermore, people living in these regions have faced serious coastal floods caused by these events for more than a half-century (Moon et al., 2003). Mokpo coastal region, located in the southwest coast of South Korea, has been hit by 58 typhoons since 1980, with most occurring in the July to October period (Kang et al., 2020; Lee et al., 2022). The rapid growth of coastal economies and populations in recent years has made these areas more susceptible to typhoon disasters. ~~The~~Therefore, the increasing frequency of typhoons on the southwestern coasts is a significant issue for disaster management.

Several studies (Halder and Bandyopadhyay, 2022; Wang et al., 2021; Shamsuzzoha et al., 2021; Kumar et al., 2021; Sadik et al., 2020; Konda et al., 2018; Parida et al., 2018; Zhang et al., 2013; Yin et al., 2013; Li and Li., 2013; Rodgers et al., 2009) have been carried out in South Asia using various techniques to map the hazard, vulnerability, risk and effects of typhoon disasters. Remote sensing and geospatial technology play a crucial role in monitoring a variety of natural disasters (Wang and Xu, 2018; Mishra et al., 2021b; Charrua et al., ~~2020~~2021). The majority of studies on typhoon-induced coastal dynamics rely on passive optical remote sensing and identify natural disaster damage using changes in landuse data, vegetation indices, and geospatial techniques (Mishra et al., 2021a; Xu et al., 2021; Nandi et al., 2020). The post-typhoon damage assessment research in South Korea mostly focused on property loss, economic losses, and casualties (Yum et al., 2021; Kim et al., 2021; Hwang et al., 2020). However, the coastal morphodynamics along the Mokpo coast over the typhoon period have not been investigated in detail. Thus, this study's primary focus is to determine the effects of typhoon Soulik on coastal ecology, landforms, erosion/accretion, suspended sediment movement and associated coastal changes along the Mokpo coast.

The normalized difference vegetation index (NDVI) and variations in NDVI (~~NDVI~~ΔNDVI) have been used to map the extent of vegetation destruction and details on the degree of damage after the typhoon (Wang et al., 2010; Datta & Deb, 2012; Zhang et al., 2013; Kumar et al., 2021; Xu et al., 2021). Vegetation damage can be seen by the negative change in NDVI values between the post-and pre-typhoon period (Mishra et al., ~~2021a; Hu & Smith, 2018).~~2021a; Hu and Smith, 2018). On the other hand, fractional vegetation coverage (FVC) is a crucial quantitative indicator of the vegetation cover of the land surface (Zhang et al., 2021; Wang and Xu, 2018; Song et al., 2017). Therefore, FVC has also been used to assess the extent of vegetation damage caused by typhoon Soulik and to analyze its impact on vegetation cover. The coastline movement over the typhoon periods has been analyzed using the Digital Shoreline Analysis System (DSAS) program (Tsai, 2022; Adhikari et al., 2021; Bishop-Taylor et al., 2021; Santos et al., 2021). In order to monitor and protect coastal habitats, we need to understand the distribution and movement of SSC between rivers and coastal waters. Thus, the ~~Normalized Difference Suspended Sediment Index~~normalized difference suspended sediment index (NDSSI) (Kavan et al., 2022; Shahzad et al., 2018; Hossain et al., 2010) and the SSC-reflectance algorithm developed by Choi et al. (2014) for the Mokpo coastal region have been used to monitor SSC distribution. Furthermore, to understand the morphodynamics of the coastal landform due to the typhoon, a GSI-based coastal change model has been developed. Four coastal landform classes, i.e., tidally influenced land (wetland land, wetland vegetation~~),~~) and non-tidally influenced land (land and water), have been used for the coastal morphodynamic analysis (Maiti and Bhattacharya, 2011). The change detection technique has been employed to quantify the pre and post-typhoon coastal changes. This approach focuses on details of morphological changes within the coast and highlights the minor changes caused by the typhoon.

This study uses Sentinel-2 MSI images as a primary data source to examine the morphodynamics and effects of Typhoon Soulik on coastal ecology. Accordingly, the objectives of this study are to (i) quantify and mapping of coastal landform dynamics prior to and after the typhoon, (ii) examine shoreline movement and assess coastal erosion and accretion, (iii) assess the degree of typhoon damage to vegetated land, and (iv) analyze changes in SSC and the response of sediment dynamics over the typhoon period. Coastal managers can use this study to develop and implement appropriate strategies and practices to protect natural ecosystems and post-disaster rehabilitation.

2. Study Area

The Mokpo coast is located in the southwestern part of South Korea and is characterized by muddy flats with wide tidal ranges (Choi et al., 2007; Kang et al., 2007), as depicted in Figure 1. The inner part of the coast includes harbor and industrial complexes, a large residential area, and a wastewater treatment plant. Mokpo coast is most frequently hit by typhoons, which cause the most significant amount of property damage and loss of human lives (Kang et al., 2020; Lee, 2014). According to storm surge records, the Mokpo coastal region has experienced the highest number of typhoons (58) since 1980 due to its geographical location (Lee et al., 2022; Kang et al., 2020). ~~It~~ The tidal range has been observed ~~that the tidal range is~~to be broader, with the extreme high tide 60cm higher and the extreme low tide 43cm lower in the Mokpo coast (Lee et al., 2022; Kwon et al., ~~2019~~2018). This fluctuation resulted in significant flooding during the typhoon period. High water and waves severely damage the coastal structures and environment, especially during surges (Tsai et al., 2006). The Mokpo coastal region is characterized by a strong ebb dominant pattern because of its complex bathymetry, scattered islands and extensive tidal flats (Byun et al., 2004; Kang and Jun, 2003; Kang, 1999).

The vast tidal flat of the Mokpo coast serves as a habitat for many different species, has a large production capacity, and is highly regarded for its role in cleaning up pollution and controlling floods and typhoons (Lee et al., 2021; Na, 2004). Furthermore, the powerful storm has affected the coastal wetlands (mudflats) that serve as the primary spawning and nursery grounds for fish and other marine life. However, Choi (2014) observed that tidal flat systems in the Korean peninsula are actively responding to various phenomena, such as tides, waves, and typhoons. The wetland, coastal vegetation and coastline along the Mokpo coastal region have been disturbed due to the extreme climatic events. It has been observed that most typhoon passages severely impacted the tidal flat environment and caused morphodynamics along the Mokpo coast.

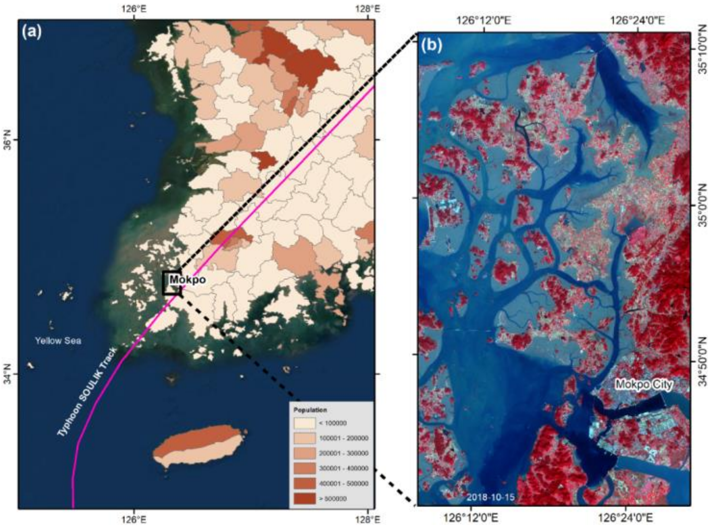
(a)
126°E
128°E
36°N
34°N
Mokpo
Yellow Sea
Typhoon SOULIK Track
Population
< 100000
100001 - 200000
200001 - 300000
300001 - 400000
400001 - 500000
> 500000
(b)
126°12'0"E
126°24'0"E
35°10'0"N
35°0'0"N
34°50'0"N
Mokpo City
2018-10-15

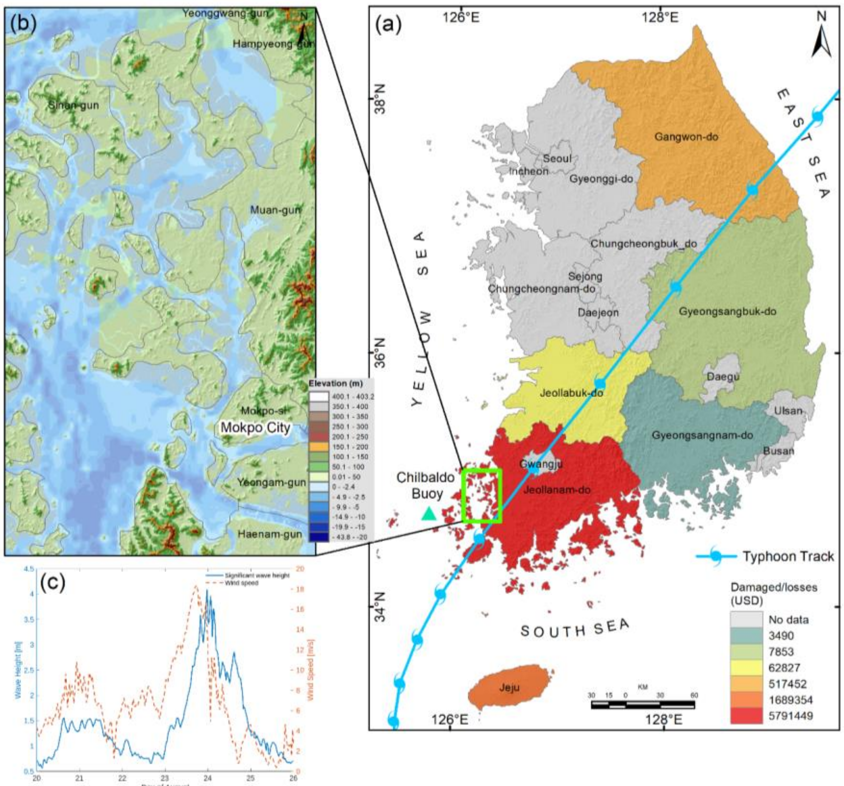
(b)
Yeonggwang-gun
Hampyeong-gun
Sinan-gun
Muan-gun
Mokpo-si
Mokpo City
Yeongam-gun
Haenam-gun
Elevation (m)
400.1 - 403.2
350.1 - 400
300.1 - 350
250.1 - 300
200.1 - 250
150.1 - 200
100.1 - 150
50.1 - 100
0.01 - 50
0 - -2.4
-4.9 - -2.5
-9.9 - -5
-14.9 - -10
-19.9 - -15
-43.8 - -20
(a)
126°E
128°E
38°N
36°N
34°N
EAST SEA
YELLOW SEA
SOUTH SEA
Seoul
Incheon
Gyeonggi-do
Gangwon-do
Chungcheongbuk_do
Sejong
Chungcheongnam-do
Daejeon
Gyeongsangbuk-do
Daegu
Jeollabuk-do
Gwangju
Jeollanam-do
Gyeongsangnam-do
Ulsan
Busan
Jeju
Chilbaldo Buoy
Typhoon Track
Damaged/losses (USD)
No data
3490
7853
62827
517452
1689354
5791449
(c)
Significant wave height
Wind speed
Wave Height [m]
Wind Speed [m/s]
Day of August

Figure 1. (a) Typhoon Soulik tracks passpassage passed through the Mokpo coastal region on 23rd August 2018 (Typhon track data iswere downloaded from https://www.ncdc.noaa.gov/ibtracs/, and basemap data are retrieved from ESRI World Imagery basemap), and https://www.ncdc. noaa.gov/ibtracs/), while the background shades represent province-wise recorded damaged/loss distribution reported by Member Report (2018), (b) The post-typhoon Standard False Colour Composite of reflectance imageTopography variation of the Mokpo coastal region (Sentinel-2 MSI level 1C satellite images areelevation data acquired from NGII (2018), https://www.ngii.go.kr/, and bathymetry data downloaded from https://scihub.copernicus.eu/dhus/GMRT, https://www.gmrt.org), and (c) Variation of significant wave height and wind speed from August 20 to 25, 2018 recorded by Chilbaldo Buoy Station (located near the landfall area) during the typhoon Soulik (Data source: http://wink.kiost.ac.kr/map/map.do#).

2.1 Typhoon Soulik

The southwestern coast of the Korean peninsula had beenwas ravaged by the strong intensity typhoon Soulik, which hit the Mokpo coast on 23rd August 2018 (Ryang et al., 20182021). On 16th August, it developed near Palau as a tropical depression. Subsequently, it strengthened into a tropical storm before intensifying into a typhoon (Lee et al., 2022). It moved into the East China Sea on 20th August with a maximum intensity of 950 hPa (44 m/s) and lasted until 22nd August. The intensity of typhoon Soulik was significantly over-predicted just before landfall on the Korean peninsula (Lee et al., 2022; Kang et al., 2020; Park et al., 2019). The Korea Meteorological Administration (KMA) issued typhoon warnings, and national and local authorities took preventative measures to limit potential damage. On 23rd August, around 14 UTC, Typhoon Soulik made landfall close to Mokpo Citycity, located on Korea's southwest coast. The typhoon remained on the mainland for an additional 12 hours before moving to the East Sea, where it underwent a transformation and became an extra-tropical cyclone. It had a maximum sustained wind speed of 3230.2 m/s observed at Gageodo in South Jeolla Province and a central pressure of 975 hPa. (Member Report, 2018). Meanwhile, the strongest gust was observed at Mt. Halla, with a peak gust of 62 m/s. It also dumped tremendous rain (KandKang and Moon, 2022; Kang et al., 2020; Yu et al., 2018; Cha et al., 2021). The buoy station near Jeju Island has recorded extreme sea surface conditions, including a maximum wave height of 15m, gusts of 35 m/s, and a drop in water temperature of 10°C. (Kang et al., 2020; Yoon et al., 2021). Furthermore, a significant wave height, i.e., 4-6 m, was also recorded along the Mokpo coast (Kang et al., 2020). In addition to causing floodingFigure 1(c) illustrates the variations in sea surface parameters between August 20 and August 25, 2018, in the vicinity of the landfall region (Chilbaldo buoy), including wind speed and significant wave height. It was observed

서식 있음: 무늬: 지우기 (흰색)
서식 있음: 무늬: 지우기 (흰색)
서식 있음: 위 첨자, 무늬: 지우기 (흰색)
서식 있음: 무늬: 지우기 (흰색)
서식 있음: 무늬: 지우기 (흰색)
서식 있음: 무늬: 지우기 (흰색)
서식 있음: 무늬: 지우기 (흰색)
서식 있음: 무늬: 지우기 (흰색)
서식 있음: 무늬: 지우기 (흰색)

that a significant wave height, i.e., 4-6 m, was recorded at Chilbaldo Buoy station. According to the Ministry of the Interior and Safety (MOIS), typhoon Soulik caused various damages and disruptions across various regions in the country. One woman was reported missing in the coastal area of Jeju, and three people sustained injuries. A total of 362 facilities were damaged. In addition, the typhoon resulted in power outages for 26,830 houses and flooding that affected over 3,063 hectares of farmland (Member Report, 2018). Furthermore, the typhoon destroyed extensive vegetation with strong gusts and damaged non-residential structures~~.~~ along the Mokpo coast. A province-wise breakdown of the damage and losses caused by the typhoon is depicted in Figure 1(a). The total damage caused by Typhoon Soulik in South Korea was $45 million (KMA, 2018).

3. Data and Methods

3.1 Data Sources and pre-processing

Typhoon-induced coastal dynamics along the Mokpo coast have been studied using the pre-and post-event Sentinel-2 MSI images. A multispectral instrument (MSI), Sentinel-2, consists of two polar-orbiting satellites, Sentinel-2A and Sentinel-2B,~~ which were~~ launched in June 2015 and March 2017, respectively (ESA, 2020). The Sentinel 2 MSI has a 290 km wide field of view, a minimum revisits period of five days, 13 spectral bands ranging from visible to shortwave infrared (SWIR), and spatial resolution of 10m (4 bands), 20m (6 bands), & 60m (3 bands) (ESA, 2020). The Sentinel-2 User Manual describes the MSI's radiometric, spectral, and spatial characteristics (ESA, 2020).

The cloud-free Sentinel-2 MSI level 1C satellite images with a relatively fine spatial resolution (10m) for the pre-and post-typhoon period have been downloaded from the Copernicus Scientific Data Hub ~~(https://scihub.copernicus.eu/dhus/).~~(https://scihub.copernicus.eu/dhus/) as depicted in Figure 2. Level 1C is a 12-bit radiometric product that was presented the top of the atmospheric reflectance value (Phiri et al., ~~2019~~2021). The open-source software SNAP (Sentinel Application Platform) has been used to process the Sentinel-2 MSI images such as masking, band visualization, atmospheric correction etc. We used SANP’s iCOR tool (image correction for atmospheric effect) for atmospheric correction of the Sentinel 2 MSI data over the land and water (Tian et al., 2020; Keukelaere et al., 2018). ~~Thereafter~~After that, satellite remote sensing reflectance (~~R_s~~R_r) images ~~have been~~were used to monitor the coastal dynamics in the Mokpo coastal region over the typhoon period.

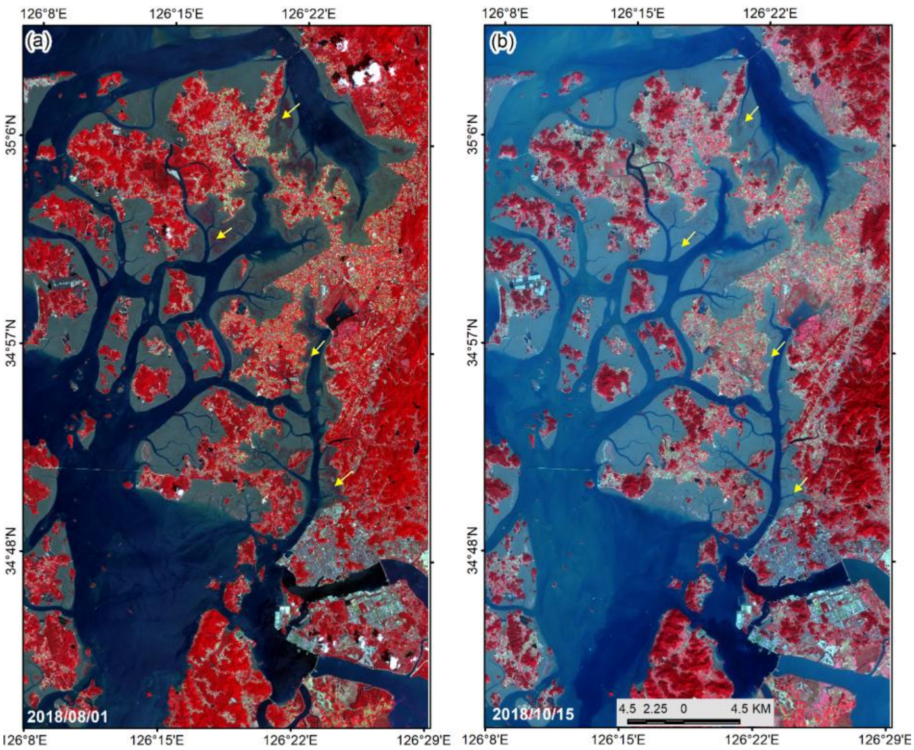

Figure 2: Pre (a) and post-typhoon (b) standard false color composite of reflectance image of the Mokpo coastal region (Sentinel-2 MSI level 1C satellite images are downloaded from https://scihub.copernicus.eu/dhus/). The arrows indicate extensive vegetation damage due to typhoon Soulik.

On the other hand, to exclude the impact of tidal changes, satellite images have been chosen during low tide conditions (Maiti and Bhattacharya, 2009). The tide height has been computed using the WXTide32 program (Hopper, 2004). Several researchers have discussed the significance of low tide satellite data for coastal mapping and dynamics modeling (Nayak, 2002). The details of pre- and post-typhoon satellite data used in the study are ~~given in Table 1.~~listed in Table 1. In addition, the coastal morphology was also investigated using high-resolution (5m×5m) topography data (i.e., LiDER DEM) provided by the Korean National Geographic Information Institute (NGII) and bathymetry data obtained from GMRT (https://www.gmrt.org) (Fig. 1b).

서식 있음: 들여쓰기: 왼쪽: 0 cm, 내어쓰기: 9.9 글자, 줄 간격: 1줄

Table 1. The details of Sentinel-2 MSI data used for coastal dynamic modeling.

Periods	Date of acquisition	Sensor	Cloud cover (%)	Tidal Height (m)
Pre-typhoon	2018/08/01	Sentinel-2B MSI	1.3464	0.77
Post-typhoon	2018/10/15	Sentinel-2B MSI	0.6548	1.01
	2019/10/20	Sentinel-2B MSI	2.8444	1.02

서식 있는 표

병합한 셀

3.2. Typhoon-induced coastal dynamic modeling

This study aims to analyze the typhoon Soulik-induced coastal dynamics and associated coastal changes along the Mokpo coastal region. Figure 23 depicts an integrated flowchart of the impact of a typhoon on a coastal system. The outline of the study is divided into four sections: (a) coastal vegetation disturbance mapping, (b) coastal landform mapping and change analysis, (c) suspended sediment concentration variation modeling, and (d) coastal erosion and accretion analysis. The details methodology of each objective has been discussed in the subsequent section.

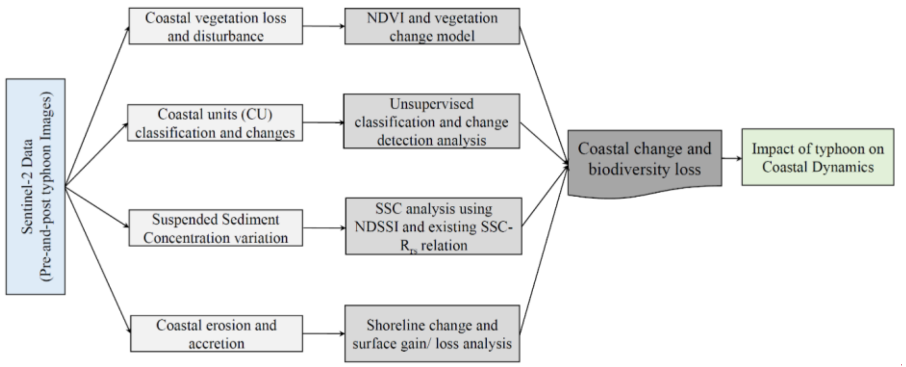

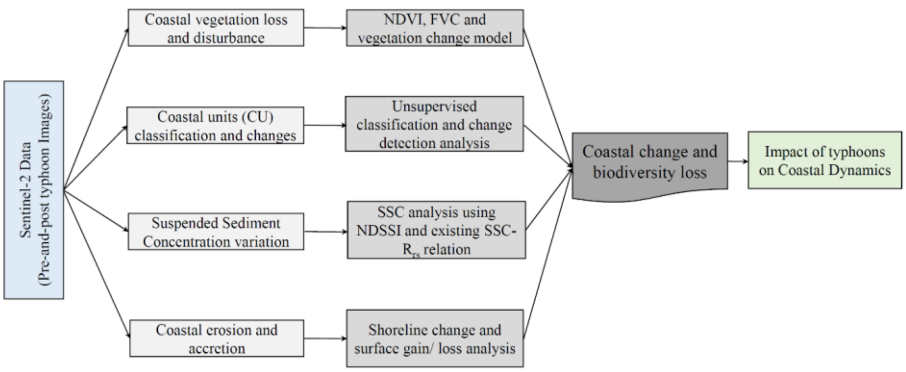

Figure ~~2~~3. Geospatial-based approach for coastal dynamics due to a typhoon.

3.2.1 Analyses of coastal vegetation loss and disturbance

Vegetation damage severity mapping (VDSM) has been performed using pre-and post-event satellite images. NDVI ~~is~~and FVC are widely used techniques for measuring vegetation density, health status, regional vegetation condition, and detecting vegetation disturbances (Xu et al., 2021; Mishra et al., 2021b; Wang et al., 2010; Yang et al., ~~2018). Numerous studies have shown that the NDVI is a reliable indicator of post-typhoon damage detection~~2018, Wang and Xu, 2018; Carlson and Ripley, 1997). Subsequently, numerous studies (Xu et al., 2021; Mishra et al., 2021a; Charrua et al., 2021; Shamsuzzoha et al., 2021; Kumar et al., 2021; Nandi et al., 2020; Wang and Xu, 2018; Konda et al., 2018; Zhang et al., 2013; Rodgers et al., 2009~~).~~) have shown that the NDVI and FVC is a reliable indicator of post-typhoon damage detection. Therefore, in this study, the vegetation damage ~~before and after Typhoon~~due to typhoon Soulik has been determined using the NDVI and FVC approach. The NDVI has been calculated by using the following Eq. (1) (Rouse et al., ~~1973~~1974; Filgueiras et al., 2019):

$$NDVI = \frac{\rho NIR - \rho RED}{\rho NIR + \rho RED} \qquad (1)$$

where~~,~~ ρNIR and ρRED are the spectral ~~reflectance~~reflectances corresponding to the ~~eight~~eighth (832.8– 832.9nm) and fourth (664.6– 664.9nm) Sentinel-2 MSI bands, respectively (Xu et al., 2021). In general, NDVI values range from -1.0 to 1.0; the higher the NDVI value, the better the conditions for vegetation development, and extremely low values indicate the presence of water. Furthermore, the NDVI value above 0.4 indicates vegetated surfaces, and those between 0.25 and 0.40 signify soils with the presence of vegetation (Charrua et al., ~~2020~~2021). The vigor of the vegetation increases as the NDVI values come closer to 1.00 (Rouse et al., 1974). Numerous studies have established the NDVI threshold for vegetated land (e.g., Xu et al., 2021; Wong et al., 2019; Liu et al., 2015; Eastman et al., 2013; Yang et al., 2012; Sobrino et al., 2004). Most researchers noted that the NDVI threshold value for vegetation cover typically ranges from 0.15-2.0 (Xu et al., 2021; Eastman et al., 2013; Sobrino et al., 2004). Therefore, the vegetated pixels (e.g., NDVI threshold > 0.20) ~~that are~~ present in pre and post-typhoon NDVI images have been used for vegetation severity analysis. The NDVI threshold is considered to reduce the influence of land cover change from the pre-typhoon (2018-08-01) to post-typhoon (2018-10-15) periods.

The degree of vegetation damage has been determined by comparing the NDVI values of the pre-and post-typhoon periods. Various researchers have frequently used the direct difference of NDVI to determine the damage severity caused by typhoons to ~~natural~~naturally vegetated land (Wang and Xu, 2018; Konda et al., 2018). It has been calculated on a cell-by-cell basis by subtracting the pre-typhoon NDVI image from that of the post-typhoon~~,~~ in ArcGIS software using map algebra (Zhang et al., 2013; Cakir et al., 2006). The following equation is used to calculate the ΔNDVI (Wang and Xu, 2018),

$$\Delta NDVI = NDVI_{post-typhoon} - NDVI_{pre-typhoon} \quad (2)$$

The difference in NDVI (i.e., ΔNDVI) illustrates the change in natural vegetation, while a negative ΔNDVI value indicates the damage inflicted by a typhoon to the vegetation cover (Xu et al., 2021).

The relative change in NDVI value has been used to investigate the geo-ecological impact on the forest area (Mishra et al., 2021b). The relative vegetation changes ($NDVI_r$) after Soulik have been determined by using the following Eq. (3) (Kumar et al., 2021~~);~~).

$$NDVI_r = \frac{\Delta NDVI}{NDVI_{pre-typhoon}} \times 100 \quad (3)$$

~~Where~~where the negative $NDVI_r$ value~~,~~ indicates vegetation loss caused by typhoons, and the positive $NDVI_r$ value shows vegetation gain. The $NDVI_r$ value has been classified into three categories corresponding to pixels with decreased, no change, or increased vegetation cover.

On the other hand, we analyze FVC in conjunction with NDVI, which provide additional insights into vegetation conditions and damage severity. Numerous researchers (Wang and Xu, 2018; Song et al., 2017; Bao et al., 2017; Chu et al., 2016; Amiri et al., 2009) used FVC to analyze vegetation damage, restoration, recovery, inter-annual variability. It is calculated as the ratio of the area covered by vegetation to the total area of the landscape. It is expressed as a percentage and can range from 0 to 100%. In the present study, FVC was calculated before and after the typhoon using the derived NDVI data (Wang and Xu, 2018). The formula of FVC is as follows (Wang and Xu, 2018; Amiri et al., 2009; Carlson and Ripley, 1997),

$$FVC = [(NDVI - NDVI_m)/(NDVI_{max} - NDVI_m)]^2 \quad (4)$$

where, $NDVI_m$ and $NDVI_{max}$ represent the $NDVI_{min}$ and $NDVI_{max}$ values calculated using equation (1) (Zhang et al., 2021; Ge et al., 2018). The calculated FVC values vary between 0 and 1. After that, the FVC values were converted to percentages to fit the actual FVC classification scheme (Wang and Xu, 2018), which consists of five classes: low (0-20%),

서식 있음: 간격 단락 뒤: 0 pt

medium-low (20-40%), medium (40-60%), medium-high (60-80%), and high (80-100%). Further, the difference in FVC values between the pre-and post-typhoon images was used to calculate the extent of vegetation damage using the following equation,

$$\Delta FVC = FVC_{post-typhoon} - FVC_{pre-typhoon} \quad (5)$$

where, ΔFVC is the difference value between the FVC before and after the typhoon. The ΔFVC value represents alterations in vegetation conditions and damage intensity, while a negative value of ΔFVC indicates the extent of damage caused by a typhoon to vegetation cover (Wang and Xu, 2018).

3.2.2 Coastal landform classification and change analysis

Typhoons have adversely affected the coastal landform and ecology of the south and west ~~coast~~coasts of the Korean peninsula every year. Therefore, a GSI-based coastal change model has been developed to understand the morphodynamics of coastal landforms during typhoons. In the present study, we considered four coastal landform classes, i.e., wetland~~ land~~, wetland vegetation, land, and water, for the coastal morphodynamic analysis (Maiti and Bhattacharya, 2011). The method consists of two algorithms, i.e., (a) the ISODATA algorithm used to classify the coastal landform with four main classes, i.e., water, wetland, wetland vegetation, and land, and (b) the change detection technique used to quantify the pre- and post-typhoon coastal changes. In this approach, we accentuate in-depth morphological changes and emphasize minor changes along the Mokpo coast caused by typhoon Soulik.

The pre-and post-typhoon Sentinel-MSI images have been classified using the unsupervised classification technique to distinguish among different coastal landforms of the study region. This approach is used to determine which types of coastal landforms were adversely affected by Typhoon Soulik and which of them have recovered more quickly than others. ~~Erdas~~ERDAS Image software has been used to run the unsupervised classification algorithm (ERDAS, 1997). Based on the k-means algorithm, this technique reduces variability within pixel clusters (Charrua et al., 2021; Aswatha et al., 2020; Bhowmik et al., 2013). Finally, pre- and post-typhoon Sentinel-2 MSI images have been classified into four coastal landform classes: land, water, wetland, and wetland vegetation.

The accuracy assessment is a commonly used method to determine how closely the classified map matches the reference ~~map~~data (Congalton, 1991). In the present study, the classified data (i.e., coastal landforms maps) have been derived through an unsupervised classification technique, while 550 random samples collected from different parts of the

Sentinel- 2MSI standard false-color image are considered reference data. Thereafter, a confusion matrix ~~has been~~was developed based on the reference and classified data to evaluate accuracy statistics (Story and Congalton, 1986). The *kappa* coefficient (*k*~~).~~) has been used to determine the quantitative accuracy of the classified map (Landis and Koch, 1977). The assessment is quantified using three different statistics: overall accuracy, producer accuracy, and user accuracy (~~Jensen, 1996).~~Story and Congalton, 1986). The model's precision is classified into five categories based on the *k* values: near perfect ($k > 0.8$), substantial ($0.6 < k < 0.8$), moderate ($0.4 < k < 0.6$), fire ($0.2 < k < 0.4$), and poor ($k < 0.2$) (Landis and Koch, 1977).

서식 있음: 글꼴: 기울임꼴

The land transformation model based on mutual spatial replacements has been applied during the post-classification stage, as shown in Figure ~~3~~4. The classified coastal landform classes, such as land, wetland, wetland vegetation, and water, have been ~~replaced~~ spatially replaced in order to create coastal-change units. For example, the coastal landform class of ~~'~~wetland ~~vegetation'~~vegetation in the pre-typhoon period replaced by ~~'water'~~water in the post-typhoon period ~~(Table 2)~~ indicates the change class ~~'~~of wetland vegetation replaced by water. A total of nine coastal-change classes have been derived, as illustrated in ~~Table 2.~~Figure 4(b).

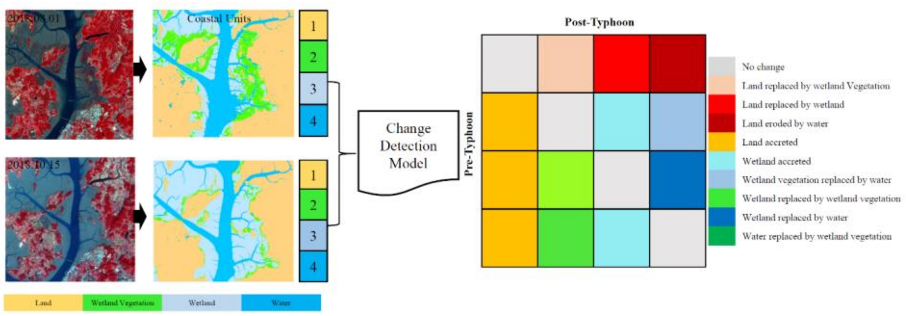

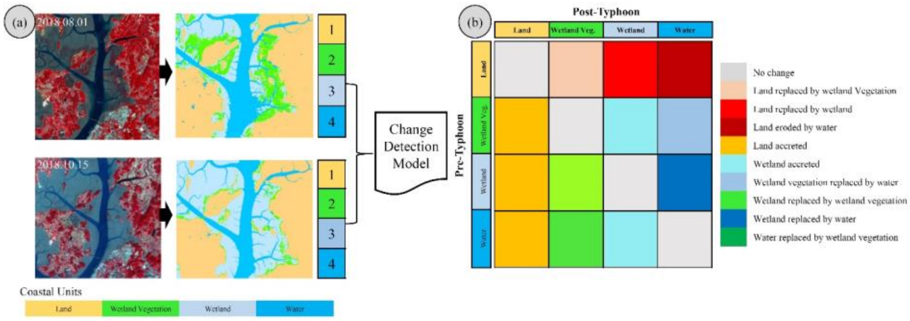

Figure ~~3~~4. The ~~Coastal~~coastal-change model exhibits ~~the~~ spatial replacements among coastal landform classes.

서식 있음: 들여쓰기: 왼쪽: 0 cm, 내어쓰기: 9.07 글자, 금칙 처리 안 함, 단어 잘림 방지, 문장 부호 끌어 맞추지 않음

~~Table 2. The coastal land transformation over the typhoon period.~~

~~Post-typhoon / Pre-typhoon~~	~~Land~~	~~Wetland Vegetation~~	~~Wetland~~	~~Water~~
~~Land~~	~~No change~~	~~Land replaced by wetland Vegetation~~	~~Land replaced by wetland~~	~~Land eroded by water~~
~~Wetland Vegetation~~	~~Land accreted~~	~~No change~~	~~Wetland accreted~~	~~Wetland vegetation replaced by water~~
~~Wetland~~	~~Land accreted~~	~~Wetland replaced by wetland vegetation~~	~~No change~~	~~Wetland replaced by water~~
~~Water~~	~~Land accreted~~	~~Water replaced by wetland vegetation~~	~~Wetland accreted~~	~~No Change~~

~~3~~3.2.3 Suspended sediment concentration modeling

The suspended sediment concentration (SSC) distribution in coastal regions is a significant indicator of changes in the marine environment caused by typhoon-induced storm surges, strong waves, and subsequent coastal flooding (Min et al., 2012; Gong and Shen, 2009). In a short period, a typhoon may drastically influence the water column structures (Souza et al., 2001), change the transport and deposition of sediment (Li et al., 2015), and affect the distribution of nutrients and biological production ~~(Wang et al., 2016)~~ in the affected seas~~.~~ (Wang et al., 2016). Extreme storms or typhoons can modify suspended sediment distribution in coastal areas, which can significantly change marine habitats (Chau et al., 2021; Lu et al., 2018; Li land Li, 2016). Due to strong typhoon wind stress, the concentration of suspended particles in the seawater column and sediment resuspension may increase dozens of times before and after the event (Lu et al., 2018; Bian et al., 2017). Thus, typhoons significantly affect suspended sediment movement in the coastal region (Zhang et al., 2022; Li and Li, 2016; Goff et al., ~~2008~~2010). The spatiotemporal distribution of SSC can be impacted by variations in tidal phase, runoff, and wind speed (Tang et al., 2021). Furthermore, the resuspension of sediment can cause numerous problems ~~to~~in ocean engineering and change the region's ecology ~~of the region~~ (Kim, 2010). The amount of material delivered to and adverted across the shelf by typhoons is considerably larger than that of winter storm systems (Dail et al., 2007). The southern and western part of the Korean peninsula is affected by an average of three typhoons annually passing through the Yellow Sea (KMA, 2018; Altman et al., 2013). Some studies on SSC distribution impacted by artificial construction along the coastal region of the Yellow Sea have been undertaken by several researchers (i.e., Lee et al., 2020; Eom et al., ~~2016~~2017; Min et al., 2012, 2014; Choi et al., 2014). However, the effects of typhoons on the sedimentary environment in the Mokpo coastal region have not yet been investigated. Therefore, it is imperative to carry out regional-scale SSC mapping and coastal modifications to reveal changes in the marine environment and sediment transport mechanisms over the typhoon period.

Remote sensing has long contributed to the advancement of water quality studies (Hossain et al., 2021). In the present study, we attempted to calculate both the qualitative and quantitative SSC in the inner-shelf region of the Mokpo coast using Sentinel-2B MSI data. The relative suspended sediment concentration has been calculated from pre- and post-typhoon Sentinel-2B MSI images using the ~~Normalized Difference Suspended Sediment Index (NDSSI).~~NDSSI. NDSSI has been used in various water quality research (Kavan et al., 2022; Hossain et al., 2010). Further, many studies (Shahzad et al., 2018; Arisanty & Saputra, 2017) have successfully used Landsat and Sentinel-2 data to calculate NDSSI~~ (Shahzad et al., 2018; Arisanty & Saputra, 2017).~~. This index determines the relative concentration of suspended sediment, with values ranging from -1 to 1, where -1 indicates the highest concentration and +1 indicates the lowest (Hossain et al. 2010). The NDSSI has been calculated by using Eq. (~~4~~6).

$$NDSSI = \frac{\rho\mathrm{Blue}-\rho\mathrm{NIR}}{\rho\mathrm{Blue}+\rho\mathrm{NIR}} \qquad (~~4~~6)$$

where~~,~~ ρBlue and ρNIR represent the surface reflectances of Band 2 (492.1– 492.4 nm) and Band 8 (832.8 – 833.0 nm) of Sentinel-2 MSI data, respectively. The NDSSI is based on the observation that turbid waters reflect more in the NIR band but less in the visible band. The negative NDSSI value represents that the reflectance of water in the NIR band is greater than that in the blue band (Shahzad et al., 2018; Hossain et al., 2010). Therefore, the positive values of NDSSI represent lower SSC or more transparent water, while a negative value indicates higher SSC. The spatial patterns of relative SSC during the typhoon period have been determined using the NDSSI.

On the other hand, the empirical model has also been used to quantify the suspended sediment concentration before and after typhoon Soulik. This method is widely used for SSC mapping and monitoring around the world (Eom et al., 2017; Hwang et al., 2016; Son et al., 2014; Min et al., 2012; Lee et al., 2011; Choi et al., 2014). For this purpose, we reviewed the existing relations between the in-situ SSC (~~SS~~SSC, g/m^3) and remote sensing reflectance (~~R_s~~R_r) developed by various researchers for the southern and western coasts of South Korea, as illustrated in Table ~~3~~2. In the present study, the SSC algorithm developed by Choi et al. (2014) for the Mokpo coastal region based on the in-situ SSC and a spectral ratio of water reflectance around 660nm has been used to quantify the SSC distribution. The atmospheric corrected sentinel-2 MSI image (~~RED~~Red band) has been used to calculate the SSC.

서식 있음: 위 첨자

Table ~~3~~2. Relationship between the remote sensing reflectance (R_r) and suspended sediment concentration (SS, g/m^3).

서식 있음: 줄 간격: 배수 1.15 줄

서식 있는 표

Authors	Relation	Region	Wavelength (nm)
Min et al. (2012) Min et al. (2006)	$Y=0.24e^{188.3x}$	Saemangeum coastal area	560nm
Choi et al. (2014)	$Y=1.545e^{179.53x}$	Mokpo coastal, Gyeonggi Bay	660nm
Lee et al. (2011)	$Y=16.2064e^{15.3529x}$	Gwangyang Bay and Yeosu Bay	565nm
Choi et al. (2012) Lee et al. (2020)	$Y=1.7532e^{204.26x}$	Yellow Sea	660nm
Eom et al. (2017)	$Y=1.5119e^{179.85x}$	Nakdong River	660nm
Min et al. (2004)	$Y=0.99e^{199.9x}$	Saemangeum	560nm

3.~~2~~.4 Coastal erosion and accretion analysis

The shorelines (i.e., land and water boundary) of the Mopko coast for pre- and post-typhoon periods have been extracted using a semi-automatic technique (Maiti and Bhattacharya, ~~2011~~2009). Here, we used the normalized difference water index (NDWI) and manual digitization approach to separate the land and water boundary. The technique is widely used for dividing ~~the~~ land and water boundary (Santos et al., 2021; Dai et al., 2019). By using Sentinel-2 imagery, NDWI can be achieved with the following formula (McFeeters, 1996),

$$NDWI = \frac{\rho Green - \rho NIR}{\rho Green + \rho NIR} \qquad (~~5~~7)$$

where~~,~~ ρGreen is the green band, and ρNIR is the near-infrared band of Sentinel-2 MSI data.

The extracted land and water boundary of the Mokpo region are then converted into polygons, and the shoreline has been determined using ArcGIS software. The shoreline change statistics have been calculated using the DSAS program (Thieler et al., 2009). The extracted shoreline for pre-and post-typhoon periods has been merged, and a 10m interval transect perpendicular to a baseline has been created (Santos et al., 2021). Thereafter, the NSM method has beenwas used to calculate the total shoreline movement (in meters) between the pre-and post-typhoon shoreline positions of each transect (Kermani et al., 2016).

$$NSM = sh_{post} - sh_{pre} \quad (68)$$

Where, $sh_{post}$where sh_{post} and sh_{pre} sh_{pre} represent the post-typhoon shoreline position and pre-typhoon shoreline positionpositions, respectively.

On the other hand, the back-shore surface area changes due to shoreline movement (retreat/advance) over the typhoon period has also been calculated using the geo-statistical analyst tool. Several researchers (Awad and El-Sayed, 2021; Deabes, 2017; Karmani et al., 2016) have also previously mapped the surface changes of the backshore region (Awad and El-Sayed, 2021; Deabes, 2017; Karmani et al., 2016).. In order to produce the surface area-change map, we generated two polygons, one for each shoreline and then subtracted them from each other over the typhoon period. using the Symmetrical Difference tool in ArcGIS software. Finally, two feature classes have been derived, one for erosion and another for accretion. In addition, the attribute table contained in each zone illustrates the magnitude of spatial changes (amounts of erosion and accretion) during the typhoon period.

4. Result and Discussion

4.1 Vegetation damage severity mapping (VDSM) before and after typhoon

4.1.1 VDSM based on the NDVI and FVC analysis

The VDSM shows the degree of vegetation damage due to typhoons. The comparison of pre-and post-typhoon NDVI and FVC distribution shows a significant loss of vegetated land as the number of no-productivity and/or low-productivity pixels increases in the post-typhoon NDVI and FVC image, as shown in ..

Figure 4.5 depicts the spatial distribution of pre and post-typhoon NDVI images. Further, to determine the severity of vegetation damage, the pre-and post-typhoon NDVI image havehas been classified into six categories, namely non-vegetation (-1.0-0.0), low-vegetation (0.0-0.2), medium-low vegetation (0.2-0.4), medium vegetation (0.4-0.6), medium-high vegetation (0.6-0.8) and high vegetation (0.8-1.0). The pre and post-typhoon mean NDVI values were observed to be 0.159 and 0.143, respectively, indicating a mean NDVI value decline of 0.016 after the typhoon.

458 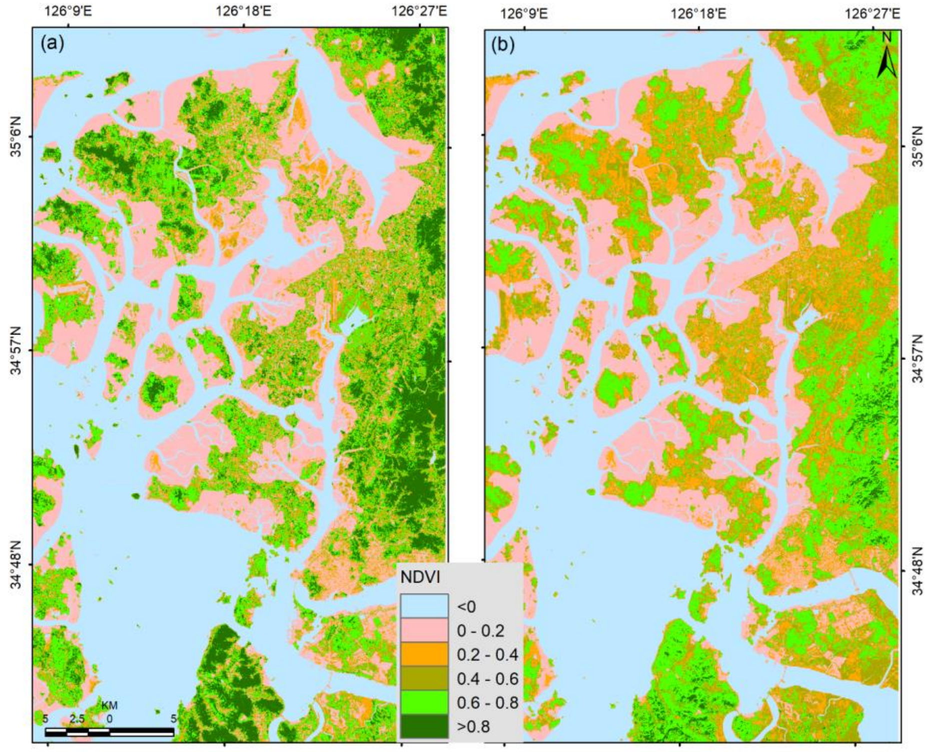
126°9'E
126°18'E
126°27'E
(a)
(b)
35°6'N
34°57'N
34°48'N
N
KM
5 2.5 0 5
NDVI
<0
0 - 0.2
0.2 - 0.4
0.4 - 0.6
0.6 - 0.8
>0.8

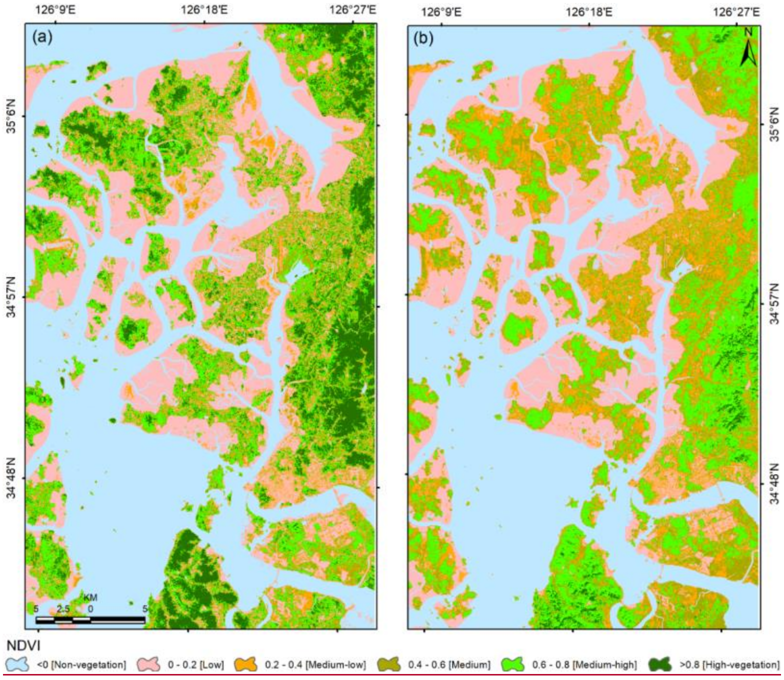

Figure ~~4~~5. Status of vegetation greenness based on the NDVI data for the (a) pre-Soulik (01st August 2018) and post-Soulik (15th October 2018) period.

Table ~~4~~3 depicts the area changes for each NDVI category ~~during~~over the typhoon period. It has been observed that the high NDVI values (>0.8) have changed drastically after typhoon-Soulik. The area changes in the ~~Low~~low and ~~Non~~non-vegetation categories along the Mokpo coastal region revealed that the wetland (mudflat) had accreted after the typhoon. On the other hand, the post-typhoon image was acquired two months after typhoon Soulik, which suggests that the grasses and crops have recovered well. This recovery is reflected in Table ~~4~~3 from medium-low to medium-high NDVI levels.

Table ~~4~~3. NDVI distribution over the study area before and after the typhoon.

NDVI levels	Pre-typhoon (~~sq.km~~km^2)	Post-typhoon (~~sq.km~~km^2)	Change (~~sq.km~~km^2)
Non-vegetation (-1 to 0)	673.~~7337~~7	647.~~5727~~6	-26.~~161~~2
Low (0 to 0.2)	430.~~0351~~4	415.~~1584~~2	-~~14.8767~~15.2
Medium-low (0.2 to 0.4)	141.~~6401~~6	243.~~2874~~3	101.~~6473~~6
Medium (0.4 to 0.6)	132.~~514~~5	225.~~3398~~3	92.~~8258~~8
Medium-high (0.6 to 0.8)	283.~~6838~~7	294.~~0909~~4	10.~~4071~~7

서식 있음: 들여쓰기: 첫 줄: 0 cm, 금칙 처리, 단어 잘림 허용, 문장 부호 끌어 맞춤
서식 있는 표
서식 있음: 왼쪽, 단어 잘림 허용
서식 있음: 왼쪽, 단어 잘림 허용
서식 있음: 왼쪽, 단어 잘림 허용
서식 있음: 왼쪽, 단어 잘림 허용
서식 있음: 왼쪽, 단어 잘림 허용

High (0.8 to 1.0)	183.~~6391~~6	19.~~7964~~8	-163.~~843~~8

서식 있음: 왼쪽, 단어 잘림 허용

On the other hand, the physical presence of vegetation has also been measured using FVC analysis. In general, NDVI provides information on the health and productivity of vegetation, while FVC provides information on the physical presence and distribution of vegetation. Figure 6 depicts the pre- and post-typhoon FVC map of the Mopko coast. The area of each FVC category is illustrated in Table 4. The results reveal that the typhoon caused a substantial decrease in FVC in the area, with the average FVC reducing significantly from 33.43% to 23.64% after the typhoon. It was observed that the medium-high to high FVC area decreased from 485.4 km^2 to 211.9 km^2, while the medium-to-low FVC area increased from 1359.8 km^2 to 1633.3 km^2. The high FVC vegetation category was more severely affected and decreased considerably after the typhoon. These results indicate that the typhoon significantly impacted the wetland vegetation in the region.

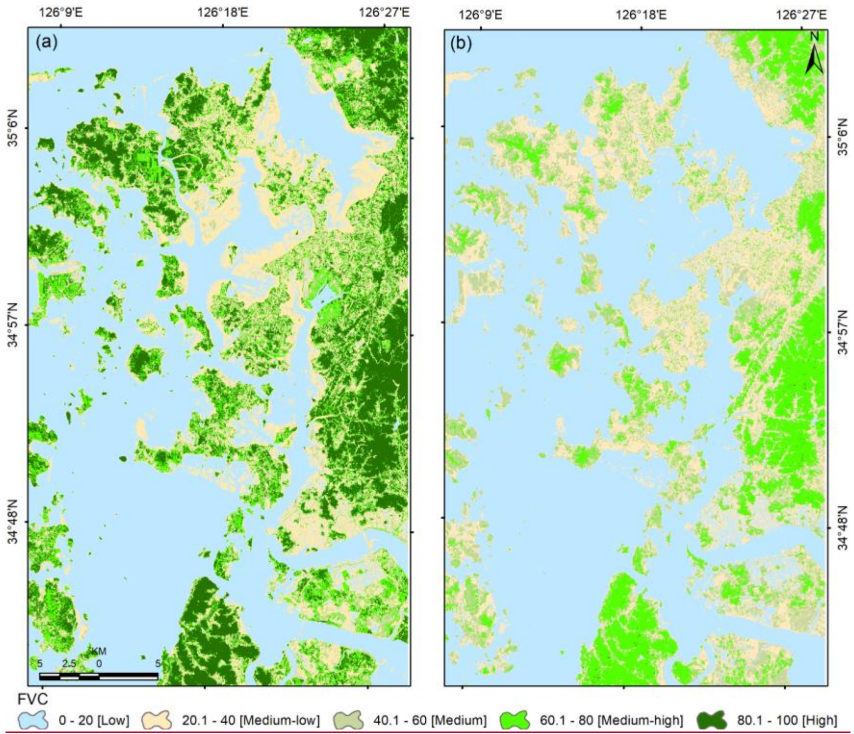

Figure 6. Status of vegetation based on the FVC analysis for the (a) pre-Soulik (01st August 2018) and post-Soulik (15th October 2018) period.

Table 4. Summary of FVC classes before and after the typhoon.

FVC levels (%)	Pre-typhoon (km^2)	Post-typhoon (km^2)	Change (km^2)
Non-vegetation (<20)	890.3	1053.3	162.943
Medium-low (20-40)	327.4	319.6	-7.811
Medium (40-60)	142.4	260.6	118.205
Medium-high (60-80)	206.1	211.5	5.365
High (80-100)	279.4	0.7	-278.671

서식 있음: 들여쓰기: 첫 줄: 0 cm, 금칙 처리 안 함, 단어 잘림 방지, 문장 부호 끌어 맞추지 않음

In order to determine the damaged vegetation areas along the Mokpo coast, we compared pre-and post-typhoon NDVI images. A decrease in ΔNDVI is one of the most distinctive features of abrupt canopy modifications detectable by optical remote sensing (Xu et al., 2021). Thus, we can only determine vegetation deterioration from the two NDVI images. Subsequently, an NDVI threshold of 0.2 has been used to extract only vegetation features from the pre-and post-typhoon NDVI images. The threshold value has been manually adjusted to achieve the highest accuracy of vegetation pixels. The extracted vegetated pixels have been compared with reference samples randomly collected from the original high spatial resolution images to determine the accuracy (Schneider, 2012; Xu et al., 2021). The two extracted vegetation images obtained within six or seven weeks of typhoon Soulik's (i.e., before the damaged vegetation had recovered) ~~resulted~~exhibits an overall accuracy of 95.7 % for pre-typhoon and 94.5% for the post-typhoon period.

Figure ~~5~~7(a) depicts the spatial distribution of ΔNDVI, where the highest ΔNDVI indicates a region with highly impacted vegetation areas. The negative ΔNDVI is attributed to about 26.7% of the total area (1845.60 km^2), which ~~indicates~~suggests that Typhoon Soulik affected approximately ~~479.9~~493.98 km^2 of vegetated land. The lowest ΔNDVI value is -0.89, which indicates either tree wind~~-throw~~ throws or a change in land surface cover from vegetation to build-up land or other non-vegetation covers (Zhang et al., 2013). The results showed that wetland vegetation and agricultural land experienced the most significant NDVI changes, with ΔNDVI values below-0.3. This suggests that these two types of land cover were severely affected by typhoon Soulik. ~~It has been observed that the vegetation covers significantly decreased after the typhoon.~~

서식 있음: 위 첨자

On the other hand, Figure 7(b) represents the change map derived from the ΔFVC, which also indicates changed vegetation areas after the typhoon. The negative ΔFVC is attributed to about 32.07% of the total area, which suggests that Typhoon Soulik affected approximately 591.89 km^2 of vegetated land. It has also been observed that the pure vegetation pixels (i.e., NDVI>0.6 and FVC>60%) were drastically changed over the typhoon period. The changed area determined for NDVI and FVC is -153.43 km^2 and -273.40 km^2, respectively (Tables 3 & 4). The results obtained from both techniques indicate a significant decrease in vegetation cover after the typhoon. The probable reason for the change is that Typhoon Soulik made landfall close to Mokpo coastal region.

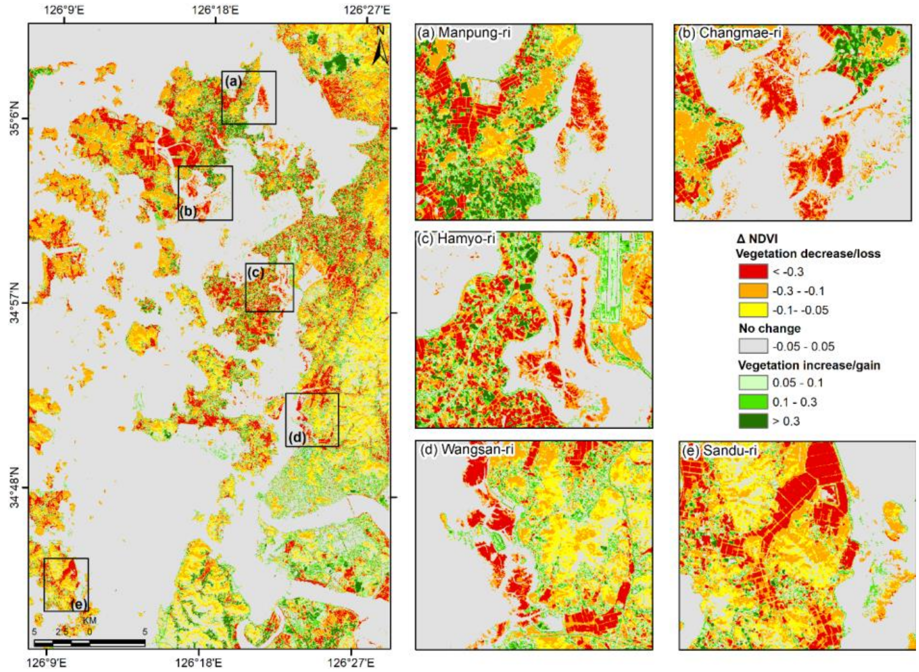

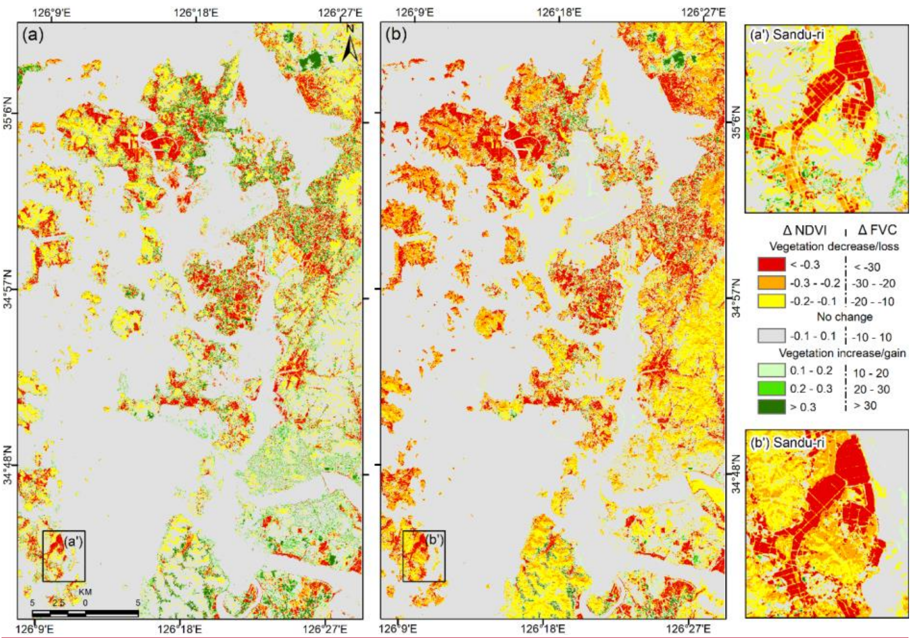

Figure ~~5. NDVI~~7. Vegetation change map ~~due to the typhoon Soulik~~ of the Mokpo coastal region derived through two different methods: (a) ΔNDVI and (b) ΔFVC, whereas zoom boxes show the vegetation damage of ~~different sites: (a) Manpung-ri, (b) Changmae-ri, (c) Hamyo-ri, (d) Wangsan-ri, and (e)~~ Sandu-ri areas.

Figure 8 compares vegetation damage based on the number and percentage of the decreased pixel of ΔNDVI and Δ FVC. It exhibits decreased pixels in different categories of vegetation damage, ranging from low damage to extensive damage. The pixels showing the most significant vegetation damage (i.e., ΔNDVI -0.2 to -0.5 and ΔFVC -20 to -50%) account for about 30.9% and 61.5% of the total pixels, respectively. On the other hand, the pixels showing extensive vegetation damage (i.e., ΔNDVI<-0.5 and ΔFVC<-50%) account for only 8.31% and 10.76% of the total pixels. It was observed that the dominant vegetation in the region is wetland vegetation, which is mainly due to the prevalence of wetlands or mudflats in the area. Therefore, the significant vegetation damage implies that wetland vegetation was most severely impacted during typhoons.

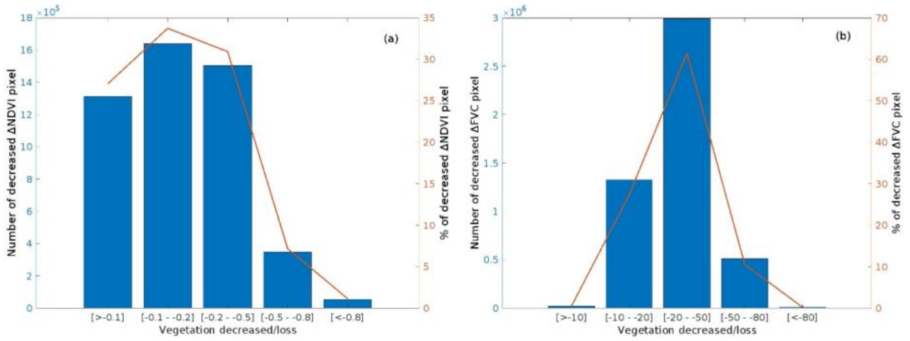

Figure 8. Comparison of vegetation damaged represented based on the number and percentage of decreased pixels of (a) ΔNDVI and (b) Δ FVC.

The pre-and post-typhoon Sentinel-2 false-color images and the corresponding relative change in $NDVI_r$ values are presented in Figure 6. The dramatic vegetation loss (<-80%) (i.e., significant loss of vegetation) occurred in mostly wetland vegetation.and ΔFVC values are presented in Figure 9. The standard FCC imagery (left panel of Fig. 9) for pre and post-typhoon shows that $NDVI_r$ is more effective in detecting areas of damaged vegetation compared to ΔFVC (right panel, Fig. 9). It was observed that the typhoon-induced damaged vegetation area (i.e., pixels with $NDVI_r$ and ΔFVC of <-50%) detected by NDVIr (106.5 km^2) was greater than that detected by ΔFVC (51.3 km^2). The difference in performance between $NDVI_r$ and ΔFVC in detecting typhoon-induced vegetation damage can be attributed to the fact that the color of the vegetation changed after the typhoon. This change can be detected more accurately by NDVI compared to FVC because the vegetation in the affected areas still existed, and vegetation coverage did not decrease significantly after the event (Wang and Xu, 2018). Thus, NDVI is highly sensitive to the health status of vegetation and a more appropriate approach for assessing the damage to vegetation induced by the typhoon, while FVC is more representative of vegetation coverage status (Wang and Xu, 2018; Jing et al., 2011). Consequently, the dramatic vegetation loss (<-80%) that occurred in mostly wetland vegetation is detected mostly in *NDVIr*. In addition, moderate greenness loss has been identified in natural forests. Furthermore, the decrease of $NDVI_r$ values from higher classes to lower classes indicates that the typhoon has severely damaged the low-lying coastal regions and the wetland vegetation.

서식 있음: 들여쓰기: 왼쪽: 0 cm, 첫 줄: 1.27 cm, 줄 간격: 1.5줄, 금칙 처리 안 함, 단어 잘림 방지, 문장 부호 끌어 맞추지 않음

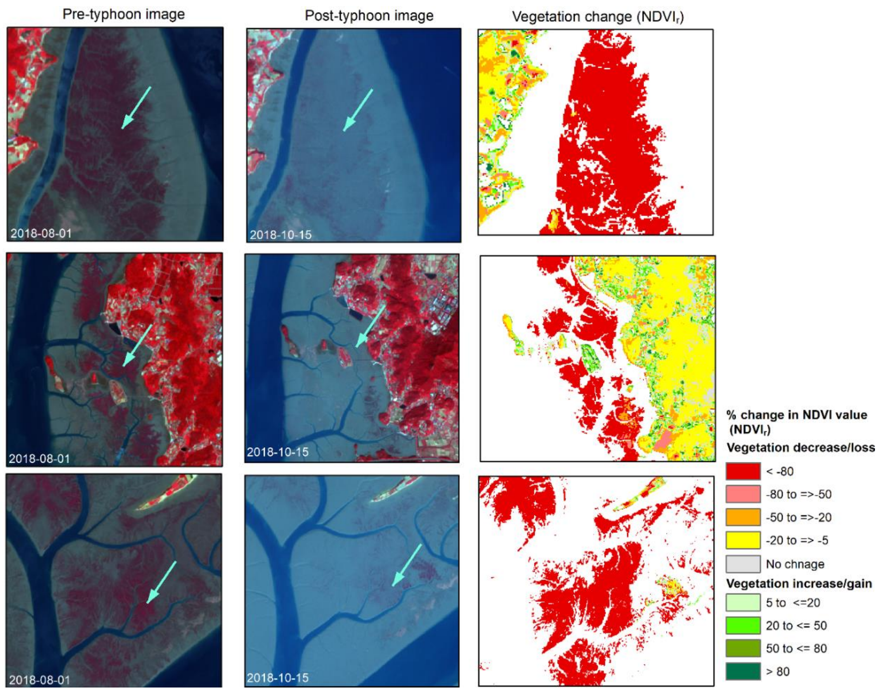
Pre-typhoon image
Post-typhoon image
Vegetation change (NDVI$_r$)
2018-08-01
2018-10-15
2018-08-01
2018-10-15
2018-08-01
2018-10-15
% change in NDVI value (NDVI$_r$)
Vegetation decrease/loss
< -80
-80 to =>-50
-50 to =>-20
-20 to => -5
No chnage
Vegetation increase/gain
5 to <=20
20 to <= 50
50 to <= 80
> 80

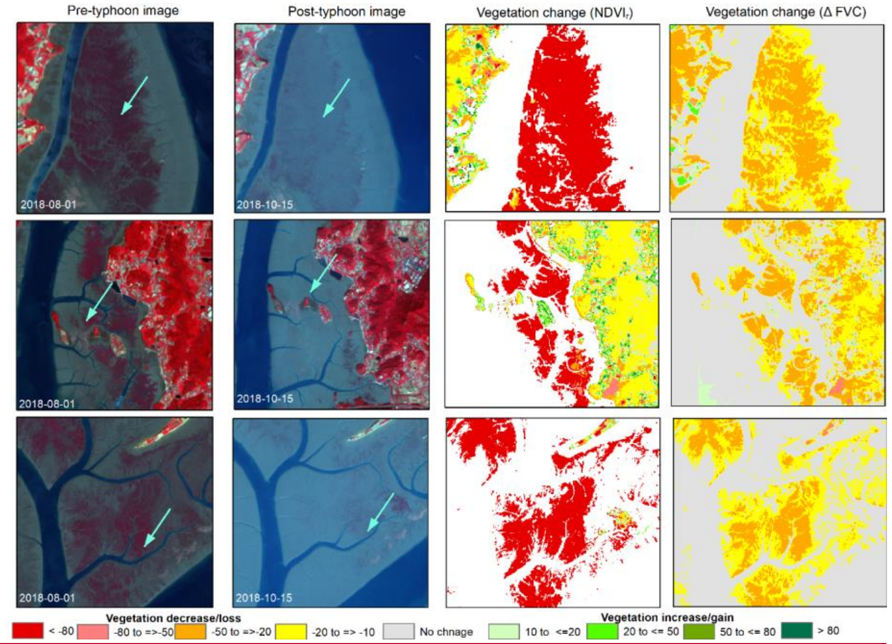

Figure ~~6~~9. Sentinel-2 MSI standard false color composite images before and after Typhoon Soulik ~~exhibits~~exhibit vegetation damage and the corresponding $NDVI_r$ and ΔFVC (Sentinel-2 MSI level 1C satellite images ~~are~~were downloaded from ~~https://scihub.copernicus.eu/dhus/~~https://scihub. copernicus.eu/dhus/).

4.1.2 Influence of topography on vegetation damage caused by Typhoon Soulik

The affected area's topography can influence typhoons' impact on vegetation. The interaction between topography and typhoon-generated wind and rain can result in complex and varied patterns of damage across different landscapes (Abbas et al., 2020; Lu et al., 2020; Zhang et al., 2013). This can affect the severity and spatial patterns of vegetation damage. Therefore, the relationship between topography and damaged vegetation has also been established in the present study. For this purpose, high-resolution (5m×5m) DEM data provided by the NGII are used to calculate the region's topographic slope and explore the relationship between topography and typhoon-induced vegetation damage.

It was observed that the elevation varies from 0 to 403 m in the Mopko coastal region, as depicted in Figure 1(b), and the number of trees damaged by Typhoon Soulik showed a decreasing trend at higher elevations (Fig. 10a). The highest number of damaged trees was observed in areas with an elevation of 50m or lower. This is likely due to the fact that these areas are predominantly covered by wetlands, which can be more vulnerable to strong winds associated with typhoons Soulik. In general, low-lying areas may not have the same natural windbreaks and barriers as higher elevations, which can exacerbate the impact of the wind. In addition, low-elevated vegetation may have shallower root systems due to the less stable soil conditions, making them more vulnerable to uprooting during heavy rainfall or strong winds (Zhang et al., 2013; Lugo et al., 1983). A significant difference in the number of decreased ΔNDVI and ΔFVC pixels was observed among different elevation ranges, and a correlation analysis between the number of damaged pixels and elevations showed a negative correlation (i.e., damaged pixels decreased with increasing elevation). The majority of damaged pixels (76.37%) were observed at elevations between 0 and 50m, with a decrease to 13.5% between 51 and 100m. Vegetation decreased rapidly at higher elevations, with the percentage of pixels with negative ΔNDVI and ΔFVC decreasing to 6.1% between 100 and 150m and decreasing to 0.02% between 350 and 403m, as depicted in Figure 10(a).

On the other hand, Figure 10(b) illustrates the extent of damaged vegetation across different slope ranges. It has been noted that there is a negative correlation between the slope and the percentage of damaged vegetation pixels, indicating that the amount of vegetation damage decreases with a higher slope. For instance, when the slope was between 0-5°, approximately 47.63% of vegetation pixels were damaged. As the slope increased, the percentage of damaged vegetation pixels decreased accordingly, with values of 18.15%, 15.01%, 10.71%, 7.74%, 0.73%, and 0.009% observed for slope ranges of 5-10°, 10-15°, 15-20°, 20-30°, 30-40°, and greater than 40°, respectively.

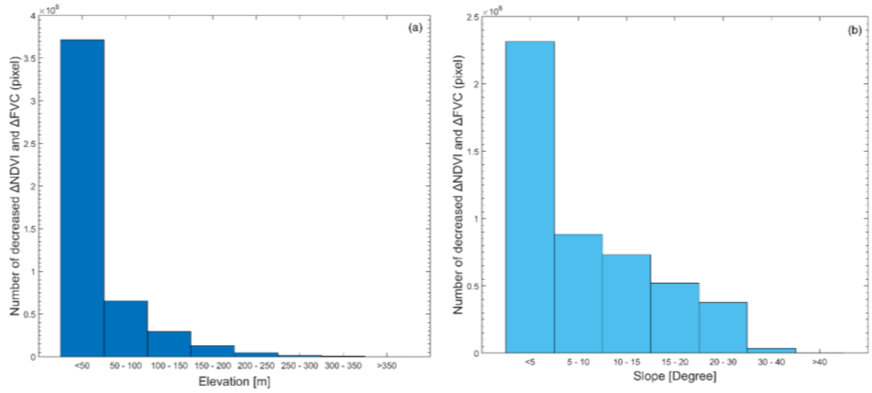

Figure 10. The relationship between topography and vegetation damaged due to typhoon Soulik: (a) numbers of damaged vegetation at different elevation ranges, and (b)

numbers of damaged vegetation at different slope ranges.

4.2 Coastal morphodynamics over the typhoon period

To understand the coastal morphodynamics over the typhoon period, we classified the entire coastal region into four major coastal landform classes: land, wetland vegetation, wetland, and water (Fig. ~~7a~~11a-b). The accuracy and *kappa* coefficient of the classified maps exhibited a reasonable degree of consistency with the reference data, as illustrated in Table 5. The overall accuracy of the pre-and post-typhoon coastal landform maps was 86.5% and 84.3%, and *kappa* coefficients were 0.82 and 0.79, respectively. The results of the coastal landform classification showed a reduction in wetland vegetation over the typhoon period. Table 6 illustrates that before the typhoon, the area of the wetland vegetation class was 4.21% (77.63 km^2) of the total area of all categories (1845.60 km^2). However, after the hitting of the typhoon storm, the wetland vegetation area reduced to 1.08~~-~~% (19.90 km^2), recording a degradation of 57.73 km^2 (-74.37%).

Table 5. Accuracy assessment of pre-and post-typhoon classified coastal units.

Coastal Units	Description	Pre-typhoon		Post-typhoon	
		Producer Accuracy (%)	User Accuracy (%)	Producer Accuracy (%)	User Accuracy (%)
Land	Others Land use	90.2	92.0	91.9	90.7
Wetland vegetation	Wetland vegetation	83.4	84.0	85.0	83.3
Wetland	Mudflat/tidal flat	81.4	84.7	77.1	74.0
Water	Waterbody	91.4	85.3	83.2	89.3
Overall accuracy (%)		86.5		84.3	
kappa		0.82		0.79	

The~~ class with the~~ most remarkable gain was the wetland class after the typhoon. This is shown by an increase of wetlands from 258.14 km^2 to 334.97 km^2, i.e., an increase of 29.76% (76.83 km^2) during the analyzed period. Furthermore, the land class has increased by only 0.20% over the typhoon period, i.e., from 45.34% (before the typhoon) to 45.44% (after the typhoon). In addition, it has been noticed the waterbody decreased by 3.09% (20.78 km^2) after the typhoon. Thus, it can be inferred that most wetland vegetation and waterbody have been converted into wetlands, which caused the coastal deterioration.

Table 6. ~~Coastal units for~~Area changes of different coastal unit during the pre- and post-

서식 있음: 글꼴: 굵게

서식 있음: 들여쓰기: 왼쪽: 0 cm, 내어쓰기: 8.06 글자, 금칙 처리 안 함, 단어 잘림 방지, 문장 부호 끌어 맞추지 않음, 탭: 3.68 글자, 왼쪽

서식 있음: 글꼴: 기울임꼴

서식 있음: 글꼴: 기울임꼴

서식 있음: 위 첨자

서식 있는 표

서식 있음: 들여쓰기: 왼쪽: 0 cm, 내어쓰기: 8.1 글자, 줄 간격: 배수 1.15 줄, 탭: 3.68 글자, 왼쪽 + 0 글자(없음)

typhoon ~~Soulik~~ periods in the Mokpo coast.

Coastal Units	Area at pre-typhoon		Area at post-typhoon		Changed area	
	~~Sq.km~~km^2	%	~~Sq.km~~km^2	%	~~Sq.km~~km^2	%
Land	836.87	45.34	838.55	45.44	1.68	0.20
Wetland Vegetation	77.63	4.21	19.90	1.08	-57.73	-74.37
Wetland	258.14	13.99	334.97	18.15	76.83	29.76
Water	672.95	36.46	652.18	35.34	-20.78	-3.09
Total	1845.60	100.00	1845.60	100.00	---	---

서식 있는 표

Thereafter, the coastal land transformation model ~~has been~~was developed through mutual spatial replacements between coastal units. ~~The~~ The land transformation model has identified the nine coastal-change units ~~have been identified through the land transformation model~~, as shown in Figure ~~7~~11(c). The results show that the low land coastal area drastically changed after the typhoon, where the majority of coastal classes have been transformed into wetlands or mudflats. Furthermore, approximately ~~9.77~~5.61% of the land area has been replaced by ~~wetland~~wetlands and water, whereas ~~65.52~~83.79% of the wetland area has accreted over the wetland vegetation and water due to the impact of typhoon Soulik (Table 7).

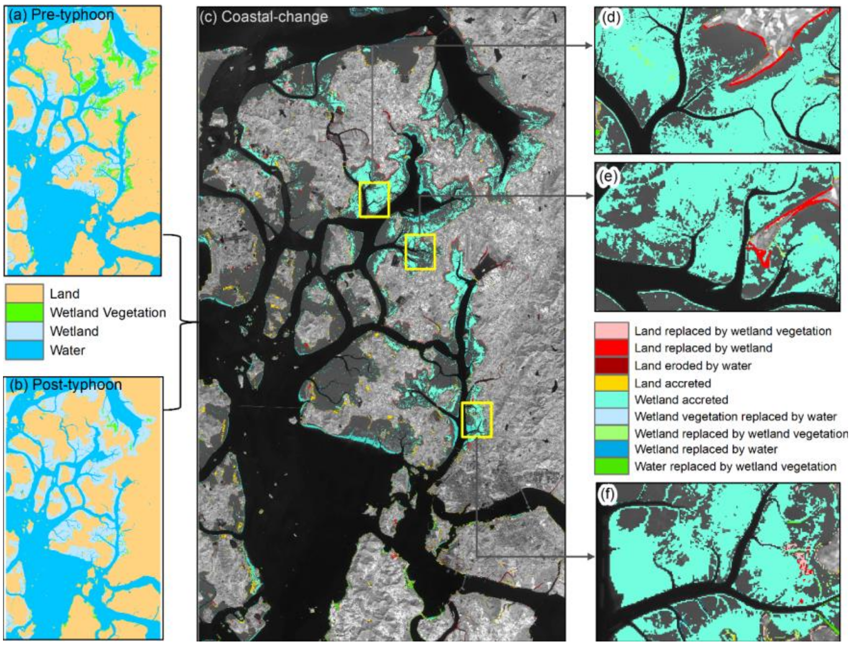

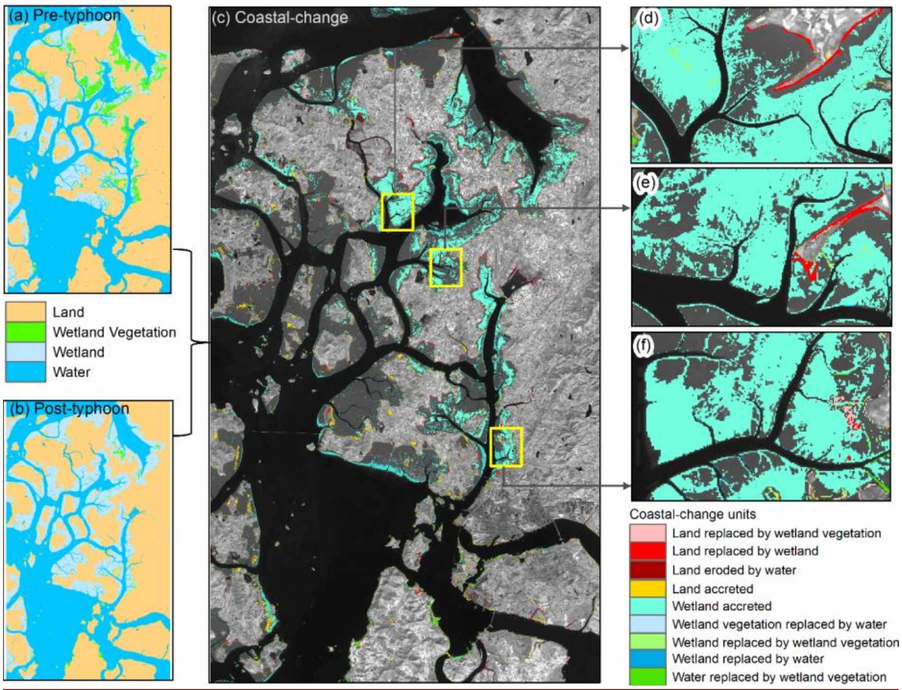

Figure ~~7~~11. Spatial distribution of coastal-change units along the Mokpo coast due to typhoon Soulik ~~(2018):~~: (a) pre-typhoon classified map, (b) post-typhoon classified map, and (c) coastal land transformation map. Subplots (d, e, and f) show the detailed coastal land transformation.

Table 7. The details of coastal land transformation classes identify over the typhoon period.

Coastal land transformation	Area (km^2)	%
Land replaced by wetland vegetation	4.59	~~6.86~~3.94
Land replaced by wetland	4.41	~~6.60~~3.79
Land eroded by water	2.12	~~3.17~~1.82
Land accreted	~~3.29~~12.88	~~4.92~~11.06
Wetland accreted	~~43~~83.79	~~65.52~~71.97
Wetland vegetation replaced by water	2.47	~~3.70~~2.12
Wetland replaced by wetland vegetation	1.59	~~2.38~~1.36
Wetland replaced by water	1.76	~~2.64~~1.52
Water replaced by wetland vegetation	2.82	~~4.22~~2.42

4.3 Sediment resuspension during the pre-and post-typhoon period

The spatial distribution of relative suspended sediment concentration has been derived

서식 있음: 글꼴: 굵게 없음

서식 있는 표

서식 있음: 위 첨자

서식 있음: 가운데, 단락의 첫 줄이나 마지막 줄 분리 허용, 단어 잘림 허용, 한글과 영어 간격을 자동으로 조절하지 않음, 한글과 숫자 간격을 자동으로 조절하지 않음

서식 있음: 가운데, 단락의 첫 줄이나 마지막 줄 분리 허용, 단어 잘림 허용, 한글과 영어 간격을 자동으로 조절하지 않음, 한글과 숫자 간격을 자동으로 조절하지 않음

서식 있음: 가운데, 단락의 첫 줄이나 마지막 줄 분리 허용, 단어 잘림 허용, 한글과 영어 간격을 자동으로 조절하지 않음, 한글과 숫자 간격을 자동으로 조절하지 않음

서식 있음: 가운데, 단락의 첫 줄이나 마지막 줄 분리 허용, 단어 잘림 허용, 한글과 영어 간격을 자동으로 조절하지 않음, 한글과 숫자 간격을 자동으로 조절하지 않음

서식 있음: 가운데, 단락의 첫 줄이나 마지막 줄 분리 허용, 단어 잘림 허용, 한글과 영어 간격을 자동으로 조절하지 않음, 한글과 숫자 간격을 자동으로 조절하지 않음

서식 있음: 가운데, 단락의 첫 줄이나 마지막 줄 분리 허용, 단어 잘림 허용, 한글과 영어 간격을 자동으로 조절하지 않음, 한글과 숫자 간격을 자동으로 조절하지 않음

서식 있음: 가운데, 단락의 첫 줄이나 마지막 줄 분리 허용, 단어 잘림 허용, 한글과 영어 간격을 자동으로 조절하지 않음, 한글과 숫자 간격을 자동으로 조절하지 않음

서식 있음: 가운데, 단락의 첫 줄이나 마지막 줄 분리 허용, 단어 잘림 허용, 한글과 영어 간격을 자동으로 조절하지 않음, 한글과 숫자 간격을 자동으로 조절하지 않음

서식 있음: 가운데, 단락의 첫 줄이나 마지막 줄 분리 허용, 단어 잘림 허용, 한글과 영어 간격을 자동으로 조절하지 않음, 한글과 숫자 간격을 자동으로 조절하지 않음

through NDSSI for both before and after typhoon images (Fig. ~~8~~12). Pre-typhoon SSC patterns have been observed more SSC inside the creeks of the inner-shelf region of the Mokpo coast as compared to the post-typhoon NDSSI image. However, it has been noted that the SSC has significantly increased along the entire coast in the post-typhoon period (Fig. ~~8b~~12b). Therefore, the spatial changes of relative SSC have been determined during the August (pre) and October (post) periods, as depicted in Figure ~~8~~12(c). In general, a flood always transports many suspended materials and concentrates those materials on the upper surface of the water. After the strong events, the flood-transported suspended material is deposited across the delta. A similar phenomenon ~~has been~~was observed in the post-typhoon period due to extensive rainfall, which turned into a coastal flood.

On the other hand, it has been observed that the SSC gradually increased as the wind speed increased from the pre to post-typhoon period. The increasing SSC amplitudes indicate the rapid sediment erosion/resuspension over the storm passage. Furthermore, the amplitudes of SSC variations were more visible in shallower water than in deeper water. The effect of typhoons on the SSC variation along the Mokpo coast has been observed through ΔNDSSI distribution (Fig. ~~8c~~12c). The negative ΔNDSSI values represent the increase of SSC due to typhoon-induced strong wind and coastal flooding.

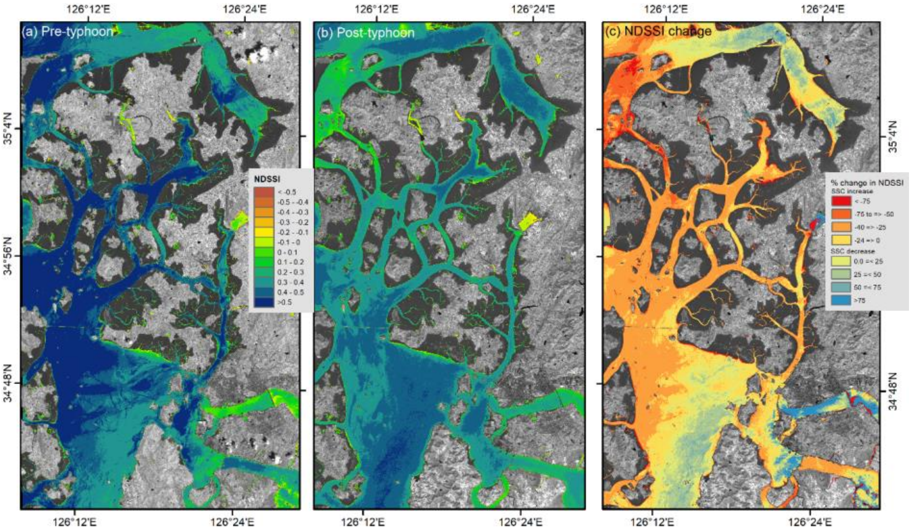

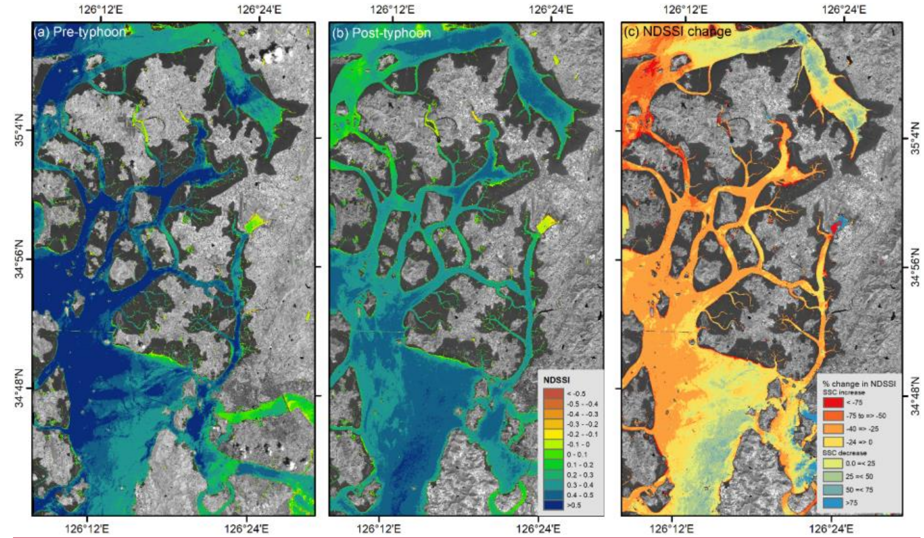

Figure ~~8~~12. Relative SSC for (a) pre-typhoon and (b) post-typhoon period, while (c) represents the changes in the NDSSI.

Furthermore, a quantitative analysis of SSC has been performed based on the algorithm developed by Choi et al. (2014). During the pre-typhoon period, the SSC in the near shore waters was significantly higher than that of the offshore region (Fig. ~~9a~~13a). The post-typhoon image shows a sharp increase in the SSC distribution, indicating that Typhoon Soulik significantly impacted the SSC variation, with a maximum of >50 g/m^3 (Fig. ~~9c~~13c). In Figures ~~9~~13(a) and (b), the spring-neap tidal influence broadly regulated the distribution and change of SSC throughout the shallow coastal water. The resuspension of SSC has been observed in the entire study region during the passage of Soulik. The pattern of relative SSC distribution (Fig. ~~8c~~12c) and the empirically derived SSC distribution (Fig. ~~9c~~13c) of pre-and post-typhoon are similar.

The outcomes showed that the storm surge and strong waves have considerably aided the sediment resuspension. Thus, the storm waves played an essential role in increasing bottom stress and stirring the seabed sediment (Gong and Shen, 2009). The transport of sediment during the storm adds another mechanism to the long-term morphological evolution of the Mokpo coast. This research revealed the profound significance of typhoons on inner shelf sedimentation along the coast.

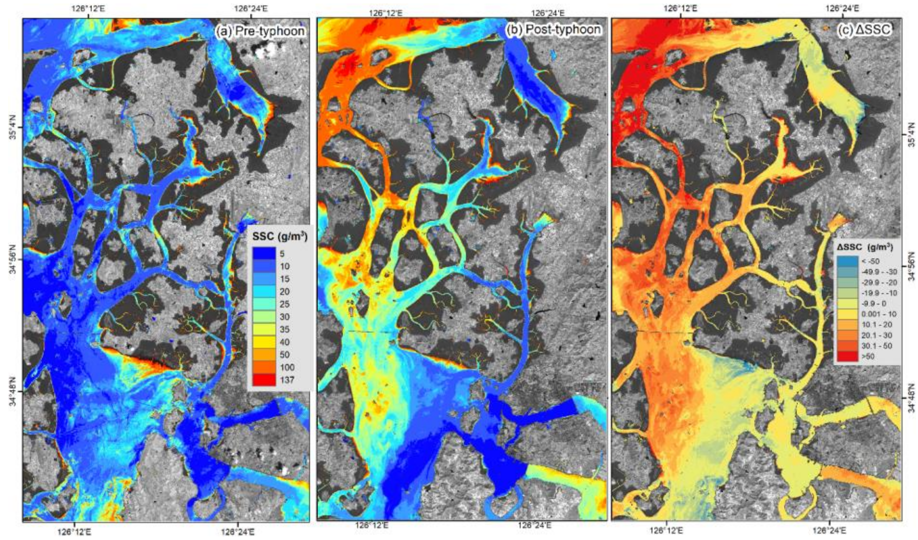

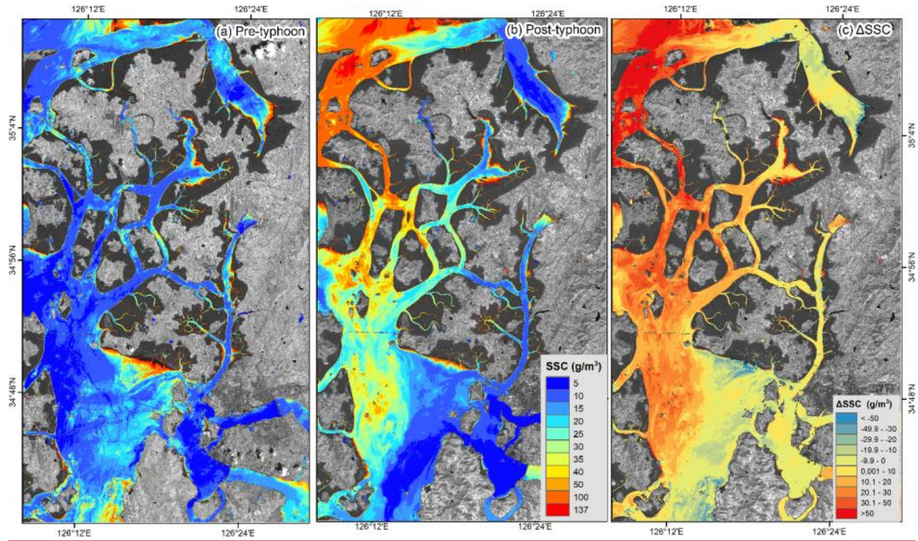

Figure ~~9~~13. The simulated SSC distribution for the surface water of (a) pre-typhoon, (b) post-typhoon period, and (c) represents the spatial changes of SSC from pre- to post-typhoon.

서식 있음: 들여쓰기: 왼쪽: 0 cm, 내어쓰기: 10.8 글자

4.4 Impact on coastal erosion and deposition

The impacts of the severe typhoon storm Soulik at a speed of ~~65 km~~62 m/s on the coastline of Mokpo have been determined using the NSM method, considering ~~37,500~~38313 transects (10m transect intervals) along the shoreline. Figure ~~10~~14 shows the shoreline alteration in the entire Mokpo coastal region from the pre- to post-typhoon period, with an accretion of 87.~~35~~5% transects and erosion of 12.~~65~~5%. The mean deposition of ~~16.98m~~28.89m and a mean erosion of -~~7.23m~~8.29m were recorded~~.~~ (Table 8). The shoreline movement between 0-10m was recorded in the northern part of the coastal region. It has been observed that most transects experienced significant accretion~~,~~; however, erosion has been observed in a few transects along the southern coastline (Fig. ~~10~~14). The southern coast experienced ~~the~~ sporadic landward movement of the shoreline~~, while~~. In contrast, the rest of the study region experienced ~~the~~ significant seaward ~~movement of the~~ shoreline movement (Fig. ~~10~~14 a-e).

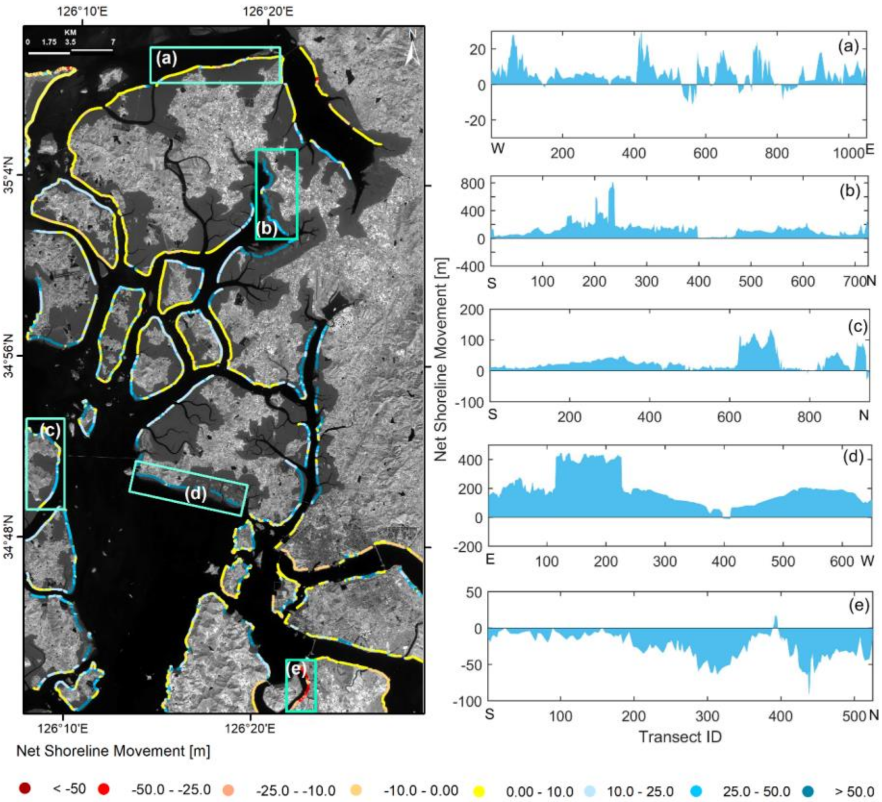

Figure ~~10~~14. Land water boundary change from the pre-typhoon period to the post-typhoon period based on the NSM method (left panel). Subplots (a-e) show the net movement of the shoreline at different sites.

Table 8. Pre-post typhoon shoreline change statistics based on the NSM model.

서식 있음: 가운데

서식 있음: 들여쓰기: 왼쪽: 0 cm, 내어쓰기: 10.8 글자

NSM statistics	Summary
Total transects	38313
NSM_{mean}	24.24m
$NSM_{mean\ accretion}$	28.89
$NSM_{mean\ erosion}$	-8.29
$NSM_{maximum\ accretion}$	812.54
$NSM_{maximum\ erosion}$	-131.72
Total transect that records accretion	34686
Total transect that records erosion	4955
% of total transect that records accretion	87.5
% of total transect that records erosion	12.5
Overall pre to post-typhoon trend	Accretion

The wind generated surface water currents that transported and dispersed erogenous material to deep seas areas from pre- to post-typhoon. On the other hand, the coastal flooding induced by the typhoon storm increased the sediment from the land to the near-shore region (Figs. ~~8c & 9c~~12c & 13c). This allowed sediment to deposit on the wetland or beach areas. The coastal land transformation map also revealed changes in shoreline shift-area as the wetland accreted class.

The net surface area changes along the coastal region have been estimated and are depicted in Figure ~~11~~15. The total beach area increases and losses throughout the typhoon period were 16.23 km^2 and 1.1 km^2, respectively (Fig. ~~11f~~15f). It ~~is~~was observed that ~~the wetland (mudflat)~~typhoon Soulik has ~~been~~ drastically increased ~~by typhoon Soulik.~~the wetland (mudflat). These observations were also supported by other proxies, as discussed above.

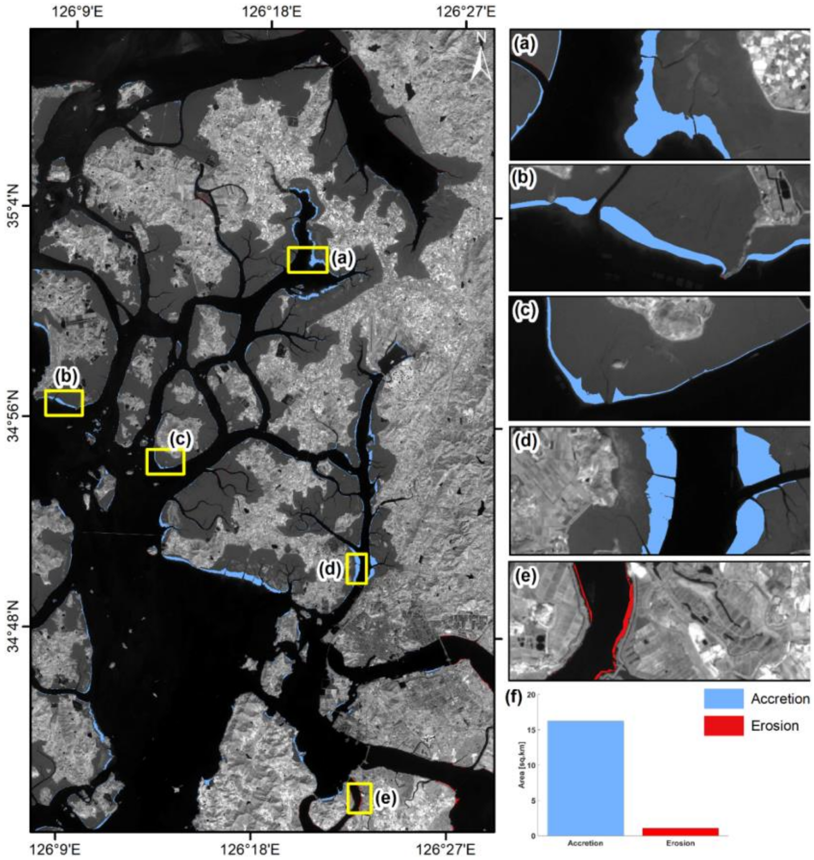

Figure ~~11. Gain and loss~~15. Net surface area changes (i.e., erosion and accretion) due to typhoon Soulik along the Mokpo coast. Subplots (a-d) show extensive accretion, while erosion is shown in plot (e). The bar graph (f) represents the area changes ~~during~~from the pre to post-typhoon period.

4.5 Coastal recovery status after typhoon Soulik

The recovery status of the Mopko coastal region after typhoon Soulik has been analyzed using the NSM and coastal landform change model. For this purpose, another Sentinel-2 MSI level 1C satellite image was downloaded for October 2019 (one year after the typhoon), as listed in Table 1. After that, the coastal landform change model and NSM were performed based on the Sentinel-2 MSI images of October 2018 and 2019 (both images taken during the post-typhoon period) to understand the recovery status of the coastal morphometry. The coastal landform change model exhibits that the wetland vegetation increased drastically after one year of typhoon Soulik, as depicted in Figure 16. Table 9 indicates that approximately 16.52% of

서식 있음: 가운데

서식 있음: 들여쓰기: 왼쪽: 0 cm, 내어쓰기: 10.8 글자

the land area has accreted over the wetland and water, whereas 39.71% of the wetland vegetation area has accreted over the wetland and water after the typhoon. Further, the outcome of the coastal recovery status was visually compared with the high-resolution aerial imagery downloaded from the National Land Information Platform web portal (https://map.ngii.go.kr/), indicating good consistency. Thus, the coastal landform change model successfully determined the longer-term recovery status in the topography and landforms of the Mopko coastal area after the typhoon.

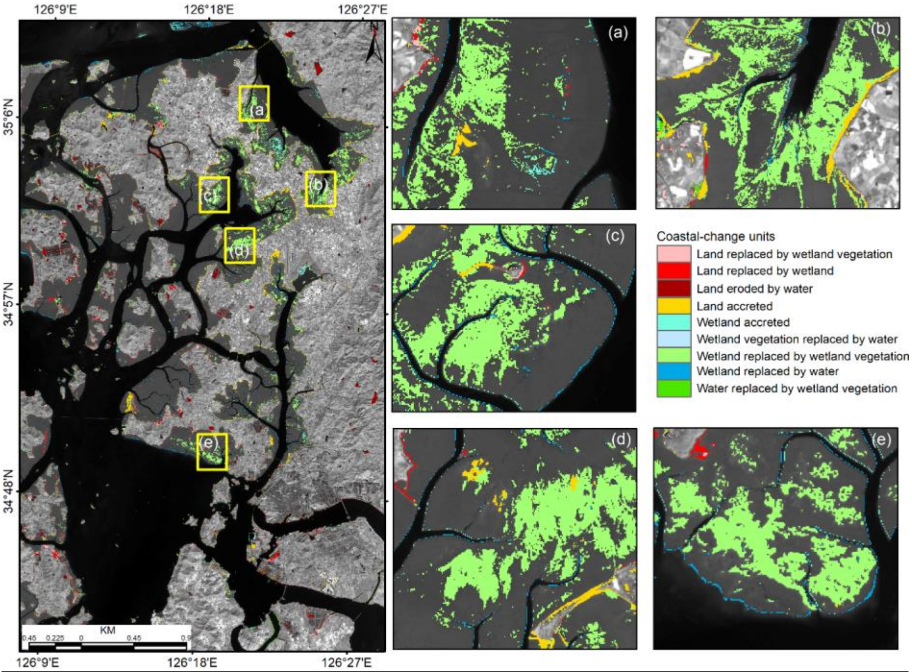

Figure 16. Recovery status of different coastal landforms after typhoon Soulik of Mokpo coastal region, whereas zoom boxes (a-e) show the increase of wetland vegetation at various sites.

Table 9. The details of coastal land transformation classes identify during the post-typhoon period.

Coastal land transformation	Area (km^2)	%
Land replaced by wetland vegetation	4.06	6.67
Land replaced by wetland	4.59	7.54
Land eroded by water	7.23	11.88
Land accreted	10.05	16.52
Wetland accreted	2.82	4.64

Wetland vegetation replaced by water	2.12	3.48
Wetland replaced by wetland vegetation	24.17	39.71
Wetland replaced by water	4.41	7.25
Water replaced by wetland vegetation	1.41	2.32

On the other hand, the short-term effects of a typhoon on the shoreline have also been determined based on the NSM model. The results exhibit the extensive shoreline alteration in the entire Mokpo coastal region after one year of typhoon Soulik, with an accretion of 48.03% transects and erosion of 51.97%. The NSM statistics showed an average shoreline movement of -1.08m, with a recorded mean erosion of -9.25 and deposition of 7.75m (Table 10). The overall erosion was recorded in response to typhoon Soulik even after one year along the Mopko coastal region. This is due to the extensive damage to wetland vegetation during the typhoon period (Table 7). In addition, it was observed that the wetland experience accretion during the typhoon period, but it made the coastline vulnerable to erosion in the near future. The natural native vegetation and wetland vegetation play a critical role in the shoreline stability of the coastal region due to its anti-erosive nature. This phenomenon was evident in the NSM statistics obtained during the post-typhoon period. Therefore, the use of these models can help predict how the shoreline and adjacent coastal landforms will respond to typhoons, identify vulnerable areas, and inform recovery efforts. This can enhance the area's resilience to natural disasters and reduce the risk of future erosion and other environmental problems.

Table 10. Post-typhoon shoreline change statistics based on the NSM model.

NSM statistics	Summary
Total transects	38313
NSM_{mean}	-1.08m
$NSM_{mean\ accretion}$	7.75
$NSM_{mean\ erosion}$	-9.25
$NSM_{maximum\ accretion}$	44.76
$NSM_{maximum\ erosion}$	-121.14
Total transect that records accretion	18400
Total transect that records erosion	19913
% of total transect that records accretion	51.97
% of total transect that records erosion	48.03
Overall pre to post-typhoon trend	Erosion

5. Conclusion

The objectives of this study were to assess the impact of ~~typhoons~~typhoon Soulik on the coastal ecology, landform, erosion/accretion, suspended sediment movement and associated coastal

서식 있음: 글꼴 색: 텍스트 1

서식 있음: 들여쓰기: 왼쪽: 0 cm, 첫 줄: 0 cm, 금칙 처리 안 함, 단어 잘림 방지, 문장 부호 끌어 맞추지 않음

changes along the Mokpo coast. This research developed an integrated approach for identifying coastal dynamics impacted by typhoons and determining damage severity. The coastline movement, coastal morphodynamics and quantified severity of vegetation damage from the pre- to post-typhoon period have been determined based on the Sentinel-2 MSI images. NDVI ~~has~~and FVC have been used to assess the severity of damage caused by typhoon Soulik on the vegetation. The results showed that about 493.9 km^2 (26.7%) of vegetation had been affected in the Mokpo coastal region. ~~However, only~~Further, it was observed that 6.1% (112.4 km^2) of vegetated areas in low coastal land were severely damaged. The land transformation model exhibited that the 'wetland' replaced most of the 'wetland-vegetated land' in the post-typhoon period. Also, it has been found that more aggregated vegetation regions were less susceptible to damage.

The SSC of the Mokpo coastal region is higher in the post-typhoon period compared to pre-typhoon time. The SSC variation influenced the coastal accretion and ~~changes~~changed the deltaic islands. The NDSSI and empirical-based SSC distribution of pre- and post-typhoon images exhibit sedimentation drastically increased after the typhoon. The land accretion process also dominated during the pre- to post-typhoon period. The wetlands and water have replaced approximately 9.77% of the land area. On the other hand, 65.52% of the wetland area has accreted over the wetland vegetation and water. Shoreline change analysis is also performed to understand erosion and accretion in coastal ~~areas. The typhoon~~regions. Typhoon Soulik accelerated shoreline movement, affecting the local environmental condition, biodiversity imbalance, and aerial change. In addition, 87.35% of shoreline transects experienced seaward migration ~~due to~~over the typhoon ~~Soulik~~period. The wetland experience accretion in a shorter period, but it made the coastline vulnerable to erosion in the near future because the natural native vegetation and wetland vegetation are crucial factors in shoreline stability of the coastal region due to its anti-erosive nature. This phenomenon was evident in the NSM and coastal landforms change model obtained during the post-typhoon period. It can be concluded that the Mokpo coastal ecosystem has been devastated by this extreme event. Although the observed changes are not alarming, shoreline protection measures still need to be addressed, especially the reforestation in wetland or mudflat regions. The outputs of the present study are needed to better understand the sediment transport process and estuary changes during the pre-and post-typhoon period. It can also be used to develop appropriate strategies to protect natural ecosystems and post-disaster rehabilitation.

Acknowledgments

This paper was supported by research funds for newly appointed professors of Gangneung-Wonju National University in 2021. The authors are thankful to the European Space Agency (ESA) for providing free satellite images. The authors would like to thank the esteemed reviewers for their valuable comments and suggestions that helped improve the manuscript.

Funding

This work was supported by the National Research Foundation of Korea (NRF) grant funded by the Korea government (NRF-2021R1C1C2003316) and Basic Science Research Program through the National Research Foundation of Korea (NRF) funded by the Ministry of Education (2021R1A6A1A03044326).

References

Abbas, S., Nichol, J. E., Fischer, G. A., Wong, M. S., and Irteza, S. M.: Impact assessment of a super-typhoon on Hong Kong's secondary vegetation and recommendations for restoration of resilience in the forest succession, Agricultural and Forest Meteorology, 280, 107784, https://doi.org/10.1016/j.agrformet.2019.107784, 2020.

Adhikari, M. D., Maiti, S., Bera, A., and Chaudhury, N. R.: Post-tsunami adjustment of coral reef platform and other morphometric changes in Landfall Island, North Andaman—An integrated field and remote sensing-based approach, Regional Studies in Marine Science, 48, 101975, https://doi.org/10.1016/j.rsma.2021.101975, 2021.

Altman, J., Doležal, J., Černý, T., and Song, J. S.: Forest response to increasing typhoon activity on the Korean peninsula: evidence from oak tree-rings, Global Change Biology, 19(2), 498-504, https://doi.org/10.1111/gcb.12067, 2013.

Amiri, R., Weng, Q., Alimohammadi, A., and Alavipanah, S. K.: Spatial–temporal dynamics of land surface temperature in relation to fractional vegetation cover and land use/cover in the Tabriz urban area, Iran, Remote sensing of environment, 113(12), 2606-2617, https://doi.org/10.1016/j.rse.2009.07.021, 2009.

Arisanty, D., and Saputra, A. N.: Remote sensing studies of suspended sediment concentration variation in Barito Delta, In IOP Conference Series: Earth and Environmental Science, 98(1), 012058, 2017.

Aswatha, S. M., Mukherjee, J., Biswas, P. K., and Aikat, S.: Unsupervised classification of land cover using multi-modal data from multispectral and hybrid-polarimetric SAR imageries, International Journal of Remote Sensing, 41(14), 5277-5304, https://doi.org/10.1080/01431161.2020.1731771, 2020.

Awad, M., and El-Sayed, H. M.: The analysis of shoreline change dynamics and future predictions using automated spatial techniques: Case of El-Omayed on the Mediterranean coast of Egypt, Ocean & Coastal Management, 205, 105568, https://doi.org/10.1016/j.ocecoaman.2021.105568, 2021.

Bao, A., Huang, Y., Ma, Y., Guo, H., and Wang, Y.: Assessing the effect of EWDP on vegetation restoration by remote sensing in the lower reaches of Tarim River, Ecological Indicators, 74, 261-275, https://doi.org/10.1016/j.ecolind.2016.11.007, 2017.

Bhowmik, A. K., and Cabral, P.: Cyclone Sidr impacts on the Sundarbans floristic diversity, Earth Science Research, 2(2), 62, http://dx.doi.org/10.5539/esr.v2n2p62, 2013.

Bhuiyan, Md. J. A. N. and Dutta, D.: Analysis of flood vulnerability and assessment of the impacts in coastal zones of Bangladesh due to potential sea-level rise, Natural Hazards, 61(2), 729-743, https://doi.org/10.1007/s11069-011-0059-3, 2012.

Bian, S., Hu, Z., Liu, J., and Zhu, Z.: Sediment suspension and the dynamic mechanism during storms in the Yellow River Delta, Environmental Monitoring and Assessment, 189(1), 1-13, https://doi.org/10.1007/s10661-016-5688-2, 2017.

Bishop-Taylor, R., Nanson, R., Sagar, S., and Lymburner, L.: Mapping Australia's dynamic coastline at mean sea level using three decades of Landsat imagery, Remote Sensing of Environment, 267, 112734, https://doi.org/10.1016/j.rse.2021.112734, 2021.

Byun, D. S., Wang, X. H., and Holloway, P. E.: Tidal characteristic adjustment due to dyke and seawall construction in the Mokpo Coastal Zone, Korea, Estuarine, Coastal and Shelf Science, 59(2), 185-196, https://doi.org/10.1016/j.ecss.2003.08.007, 2004.

Cakir, H. I., Khorram, S., and Nelson, S. A.: Correspondence analysis for detecting land cover change, Remote Sensing of Environment, 102 (3-4), 306-317, https://doi.org/10.1016/j.rse.2006.02.023, 2006.

Carlson, T. N., and Ripley, D. A.: On the relation between NDVI, fractional vegetation cover, and leaf area index, Remote sensing of Environment, 62(3), 241-252, https://doi.org/10.1016/S0034-4257(97)00104-1, 1997.

Cha, E. J., Yun, S. G., Moon, I. J., and Kim, D. H.: Binary interaction of typhoons Soulik and Cimaron in 2018–Part I: Observational characteristics and forecast error, Tropical Cyclone Research and Review, 10(1), 32-42, https://doi.org/10.1016/j.tcrr.

2021.03.001, 2021.

Charrua, A. B., Padmanaban, R., Cabral, P., Bandeira, S., and Romeiras, M. M.: Impacts of the tropical cyclone idai in mozambique: A multi-temporal Landsat satellite imagery analysis, Remote Sensing, 13(2), 201, https://doi.org/10.3390/rs13020201, 2021.

Chau, P. M., Wang, C. K., and Huang, A. T.: The spatial-temporal distribution of GOCI-derived suspended sediment in Taiwan coastal water induced by typhoon Soudelor, Remote Sensing, 13(2), 194, https://doi.org/10.3390/rs13020194, 2021.

Choi, M. K., Choi, H. G., Moon, H. B., Yu, J., Kang, S. K., and Choi, S. K.: Sources and distributions of organic wastewater compounds on the Mokpo Coast of Korea, Fisheries and Aquatic Sciences, 10(4), 205-214, https://doi.org/10.5657/fas.2007.10.4.205, 2007.

Choi, J. K., Park, Y. J., Ahn, J. H., Lim, H. S., Eom, J., and Ryu, J. H.: GOCI, the world's first geostationary ocean color observation satellite, for the monitoring of temporal variability in coastal water turbidity, Journal of Geophysical Research: Oceans, 117(C9), https://doi.org/10.1029/2012JC008046, 2012.

Choi, J. K., Park, Y. J., Lee, B. R., Eom, J., Moon, J. E., and Ryu, J. H.: Application of the Geostationary Ocean Color Imager (GOCI) to mapping the temporal dynamics of coastal water turbidity, Remote Sensing of Environment, 146, 24-35, https://doi.org/10.1016/j.rse.2013.05.032, 2014.

Choi, K.: Morphology, sedimentology and stratigraphy of Korean tidal flats–Implications for future coastal managements, Ocean & Coastal Management, 102, 437-448, https://doi.org/10.1016/j.ocecoaman.2014.07.009, 2014.

Chu, T., Guo, X.,and Takeda, K.: Remote sensing approach to detect post-fire vegetation regrowth in Siberian boreal larch forest, Ecological Indicators, 62, 32-46, https://doi.org/10.1016/j.ecolind.2015.11.026, 2016.

Congalton, R. G.: A review of assessing the accuracy of classifications of remotely sensed data, Remote Sensing of Environment, 37(1), 35-46, https://doi.org/10.1016/0034-4257(91)90048-B, 1991.

Dai, C, Howat, I. M., Larour, E., and Husby, E.: Coastline extraction from repeat high resolution satellite imagery, Remote Sensing of Environment, 229, 260–270, https://doi.org/10.1016/j.rse.2019.04.010, 2019.

Dail, M. B., Corbett, D. R., and Walsh, J. P.: Assessing the importance of tropical cyclones on continental margin sedimentation in the Mississippi delta region, Continental Shelf Research, 27(14), 1857-1874, https://doi.org/10.1016/j.csr.2007.03.004, 2007.

Datta, D. and Deb, S.: Analysis of coastal land use/land cover changes in the Indian Sunderbans using remotely sensed data, Geospatial Information Science, 15(4), 241-250, https://doi.org/10.1080/10095020.2012.714104, 2012.

Deabes, E. A.: Applying ArcGIS to Estimate the Rates of Shoreline and Back-Shore Area Changes along the Nile Delta Coast, Egypt, International Journal of Geosciences, 8(03), 332, DOI: 10.4236/ijg.2017.83017, 2017.

Eastman, J. R., Sangermano, F., Machado, E. A., Rogan, J., and Anyamba, A.: Global trends in seasonality of normalized difference vegetation index (NDVI), 1982–2011, Remote Sensing, 5(10), 4799-4818, https://doi.org/10.3390/rs5104799, 2013.

Eom, J., Lee, C., Jang, J., Choi, J. K., and Park, S.: Study on environmental change monitoring between shoreline change and suspended sediment concentration using Landsat images in Nakdong river, Korea, In IEEE International Geoscience and Remote Sensing Symposium (IGARSS), 3607-3609, 2017.

ERDAS.: ERDAS Imagine Tour Guides (Atlanta, GA: ERDAS Inc.), 1997.

ESA.: Multispectral instrument (MSI) overview, Retrieved 07th September, 2022, from https://sentinels.copernicus.eu/web/sentinel/technical-guides/sentinel-2-msi, 2020.

Filgueiras, R., Mantovani, E. C., Althoff, D., Fernandes Filho, E. I., and Cunha, F. F. D.: Crop NDVI monitoring based on sentinel 1, Remote Sensing, 11(12), 1441, https://doi.org/10.3390/rs11121441, 2019.

Ge, J., Meng, B., Liang, T., Feng, Q., Gao, J., Yang, S., ... and Xie, H.: Modeling alpine grassland cover based on MODIS data and support vector machine regression in the headwater region of the Huanghe River, China, Remote Sensing of Environment, 218, 162-173, https://doi.org/10.1016/j.rse.2018.09.019, 2018.

Goff, J. A., Allison, M. A., and Gulick, S. P.: Offshore transport of sediment during cyclonic storms: Hurricane Ike (2008), Texas Gulf Coast, USA, Geology, 38(4), 351-354, https://doi.org/10.1130/G30632.1, 2010.

Gong, W. and Shen, J.: Response of sediment dynamics in the York River Estuary, USA to tropical cyclone Isabel of 2003, Estuarine, Coastal and Shelf Science, 84(1), 61-74, https://doi.org/10.1016/j.ecss.2009.06.004, 2009.

Halder, B. and Bandyopadhyay, J.: Monitoring the tropical cyclone 'Yass' and 'Amphan'affected flood inundation using Sentinel-1/2 data and Google Earth Engine, Modeling Earth Systems and Environment, 1-16, https://doi.org/10.1007/s40808-022-01359-w, 2022.

Hopper, M.: WXTide32 Version 4.0. Free Software Foundation Inc., Cambridge, 2004.
Hoque, M. A. A., Phinn, S., Roelfsema, C., and Childs, I.: Assessing tropical cyclone impacts using object-based moderate spatial resolution image analysis: a case study in Bangladesh, International Journal of Remote Sensing, 37(22), 5320-5343, https://doi.org/10.1080/01431161.2016.1239286, 2016.
Hossain, A. K. M. A., Jia, Y., and Chao, X.: Development of remote sensing based index for estimating/mapping suspended sediment concentration in river and lake environments, In Proceedings of 8th international symposium on ECOHYDRAULICS, 435, 578-585, 2010.
Hossain, A. A., Mathias, C., and Blanton, R.: Remote sensing of turbidity in the Tennessee River using Landsat 8 satellite, Remote Sensing, 13(18), 3785, https://doi.org/10.3390/rs13183785, 2021.
Hu, T. and Smith, R. B.: The impact of Hurricane Maria on the vegetation of Dominica and Puerto Rico using multispectral remote sensing, Remote Sensing, 10(6), 827, https://doi.org/10.3390/rs10060827, 2018.
Hwang, D. J., Choi, J. K., Eom, J., Ryu, J. H., and Woo, H. J.: Long-term monitoring of suspended sediments concentration using GOCI and field data in Han-river estuary, Korea, In 2016 IEEE International Geoscience and Remote Sensing Symposium, 2465-2467, 2016.
Hwang, S., Son, S., Lee, C., and Yoon, H. D.: Quantitative assessment of inundation risks from physical contributors associated with future storm surges: a case study of Typhoon Maemi (2003), Natural Hazards, 104(2), 1389-1411, https://doi.org/10.1007/s11069-020-04225-z, 2020.
Jing, X., Yao, W. Q., Wang, J. H., and Song, X. Y.: A study on the relationship between dynamic change of vegetation coverage and precipitation in Beijing's mountainous areas during the last 20 years, Mathematical and Computer Modelling, 54(3-4), 1079-1085, https://doi.org/10.1016/j.mcm.2010.11.038, 2011.
Kang, J. W.: Changes in tidal characteristics as a result of the construction of sea-dike/sea-walls in the Mokpo coastal zone in Korea, Estuarine, Coastal and Shelf Science, 48 (4), 429-438, https://doi.org/10.1006/ecss.1998.0464, 1999.
Kang, J. W. and Jun, K. S.: Flood and ebb dominance in estuaries in Korea, Estuarine, Coastal and Shelf Science, 56 (1), 187-196, https://doi.org/10.1016/S0272-7714(02)00156-7, 2003.

Kang, J. W., Moon, S. R., Lee, D. S., and Lee, J. L.: Surge-Wave Combined Inundation at Mokpo North Harbour, Korea, Journal of Coastal Research, 1081-1085, 2007.

Kang, K., Jo, H. J., and Kim, Y.: Ocean responses to Typhoon Soulik (1819) around Korea, Ocean Science Journal, 55(3), 445-457, https://doi.org/10.1007/s12601-020-0030-x, 2020.

Kang, K. and Moon, I. J.: Sea Surface Height Changes due to the Tropical Cyclone-Induced Water Mixing in the Yellow Sea, Korea, Frontiers of Earth Science, 10, 826582, doi: 10.3389/feart.2022.826582, 2022.

Kavan, J., Wieczorek, I., Tallentire, G. D., Demidionov, M., Uher, J., and Strzelecki, M. C.: Estimating Suspended Sediment Fluxes from the Largest Glacial Lake in Svalbard to Fjord System Using Sentinel-2 Data: Trebrevatnet Case Study, Water, 14(12), 1840, https://doi.org/10.3390/w14121840, 2022.

Kermani, S., Boutiba, M., Guendouz, M., Guettouche, M. S., and Khelfani, D.: Detection and analysis of shoreline changes using geospatial tools and automatic computation: Case of jijelian sandy coast (East Algeria), Ocean & Coastal Management, 132, 46-58, https://doi.org/10.1016/j.ocecoaman.2016.08.010, 2016.

Keukelaere, L. De, Sterckx, S., Adriaensen, S., Knaeps, E., Reusen, I., Giardino, C., ... and Vaiciute, D.: Atmospheric correction of Landsat-8/OLI and Sentinel-2/MSI data using iCOR algorithm: validation for coastal and inland waters, European Journal of Remote Sensing, 51(1), 525-542, https://doi.org/10.1080/22797254.2018.1457937, 2018.

Kim, Y. C.: Handbook of coastal and ocean engineering, World Scientific, 2010.

Kim, J. M., Bae, J., Son, S., Son, K., and Yum, S. G.: Development of model to predict natural disaster-induced financial losses for construction projects using deep learning techniques. Sustainability, 13(9), 5304, https://doi.org/10.3390/su13095304, 2021.

KMA.: Typhoon White Book, Available at https://www.kma.go.kr/download_01/typhoon/typwhitebook_2011.pdf, 2011.

KMA.: 2018 annual report, available at https://www.kma.go.kr/download_01/Annual_Report_2018.pdf , 2018.

Konda, V. G. R. K., Chejarla, V. R., Mandla, V. R., Voleti, V., and Chokkavarapu, N.: Vegetation damage assessment due to Hudhud cyclone based on NDVI using Landsat-8 satellite imagery, Arabian Journal of Geosciences, 11(2), 1-11, https://doi.org/10.1007/s12517-017-3371-8, 2018.

Kumar, R., Rani, S., and Maharana, P.: Assessing the impacts of Amphan cyclone over West

Bengal, India: a multi-sensor approach, Environmental Monitoring and Assessment, 193(5), 1-21, https://doi.org/10.1007/s10661-021-09071-5, 2021.

Kwon, J. I., Choi, J. W., Lee, J. C., Min, I. K., and Park, K. S.: Spatio-temporal Characteristics of Storm Surge Events in the Korean Peninsula, Journal of Coastal Research, 85 (10085), 891-895, 2018.

Landis, J. R. and Koch, G. G.: An application of hierarchical kappa-type statistics in the assessment of majority agreement among multiple observers, Biometrics, 363-374, 1977.

Lee, J. K., Kim, J. O., and Oh, Y. S.: Development of Coastal Safety Mapping System by Vulnerability Assessment of Tidal Creeks, Journal of Coastal Research, 114, 459-463, 2021.

Lee, M. S., Park, K., Chung, J. Y., Ahn, Y. H., and Moon, J. E.: Estimation of coastal suspended sediment concentration using satellite data and oceanic in-situ measurements, Korean Journal of Remote Sensing, 27(6), 677-692, 2011.

Lee, S. W., Nam, S. H., and Kim, D. J.: Estimation of marine winds in and around typhoons using multi-platform satellite observations: Application to Typhoon Soulik (2018), Frontiers of Earth Science, 16(1), 175-189, https://doi.org/10.1007/s11707-020-0849-6, 2022.

Lee, Y.: 2014. Coastal planning strategies for adaptation to sea level rise: A case study of Mokpo, Korea, Journal of Building Construction and Planning Research, 2(1), DOI:10.4236/jbcpr.2014.21007, 2014.

Lee, Y. K., Choi, J. K., and Lee, H. J.: A study on seasonal dynamics of suspended particulate matter in Korean coastal waters using GOCI, Journal of Coastal Research, 102 (SI), 232-245, https://doi.org/10.2112/SI102-029.1, 2020.

Li, K. and Li, G. S.: Risk assessment on storm surges in the coastal area of Guangdong Province, Natural Hazards, 68(2), 1129-1139, https://doi.org/10.1007/s11069-013-0682-2, 2013.

Li, Y., Li, H., Qiao, L., Xu, Y., Yin, X., and He, J.: Storm deposition layer on the Fujian coast generated by Typhoon Saola (2012), Scientific reports, 5(1), 1-7, https://doi.org/10.1038/srep14904, 2015.

Li, Y. and Li, X.: Remote sensing observations and numerical studies of a super typhoon-induced suspended sediment concentration variation in the East China Sea, Ocean Modelling, 104, 187-202, https://doi.org/10.1016/j.ocemod.2016.06.010, 2016.

Liu, Y., Wu, L., and Yue, H.: Biparabolic NDVI-Ts space and soil moisture remote sensing in an arid and semi-arid area, Canadian Journal of Remote Sensing, 41(3), 159-169, https://doi.org/10.1080/07038992.2015.1065705, 2015.

Lu, J., Jiang, J., Li, A., and Ma, X.: Impact of Typhoon Chan-hom on the marine environment and sediment dynamics on the inner shelf of the East China Sea: In-situ seafloor observations, Marine Geology, 406, 72-83, https://doi.org/10.1016/j.margeo.2018.09.009, 2018.

Lu, L., Wu, C., and Di, L.: Exploring the spatial characteristics of typhoon-induced vegetation damages in the southeast coastal area of China from 2000 to 2018, Remote Sensing, 12(10), 1692, https://doi.org/10.3390/rs12101692, 2020.

Lugo, A. E., Applefield, M., Pool, D. J., and McDonald, R. B.: The impact of Hurricane David on the forests of Dominica, Canadian Journal of Forest Research, 13(2), 201-211, https://doi.org/10.1139/x83-029, 1983.

Maiti, S., and Bhattacharya, A. K.: Shoreline change analysis and its application to prediction: A remote sensing and statistics based approach, Marine Geology 257(1-4), 11-23, https://doi.org/10.1016/j.margeo.2008.10.006, 2009.

Maiti, S. and Bhattacharya, A. K.: A three-unit-based approach in coastal-change studies using Landsat images, International Journal of Remote Sensing, 32(1), 209-229, https://doi.org/10.1080/01431160903439965, 2011.

Mallick, B., Ahmed, B., and Vogt, J.: Living with the risks of cyclone disasters in the southwestern coastal region of Bangladesh, Environments, 4(1), 13, https://doi.org/10.3390/environments4010013, 2017.

McFeeters, S. K.: The use of the Normalized Difference Water Index (NDWI) in the delineation of open water features, International Journal of Remote Sensing, 17(7), 1425–1432, https://doi.org/10.1080/01431169608948714, 1996.

Member Report: Member Report, Republic of Korea. ESCAP/WMO Typhoon Committee, 13th Integrated Workshop, Chiang Mai, Thailand, 5-9 November 2018 (Avialable at https://www.typhooncommittee.org/13IWS/Members13IWS.html, lat access 28th April, 2023), 2018.

Min, J. E., Ryu, J. H., Ahn, Y. H., and Lee, K. S.: Monitoring suspended sediment distribution using Landsat TM/ETM+ data in coastal waters of Seamangeum, Korea, In Proceedings of the KSRS Conference, The Korean Society of Remote Sensing, 340-343, 2004.

Min, J. E., Ahn, Y. H., Lee, K. S., and Ryu, J. H.: Development of Suspended Sediment

Algorithm for Landsat TM/ETM+ in Coastal Sea Waters-A Case Study in Saemangeum Area, Korean Journal of Remote Sensing, 22(2), 87-99, 2006.
Min, J. E., Ryu, J. H., Lee, S., and Son, S.: Monitoring of suspended sediment variation using Landsat and MODIS in the Saemangeum coastal area of Korea, Marine Pollution Bulletin, 64(2), 382-390, https://doi.org/10.1016/j.marpolbul.2011.10.025, 2012.
Min, J. E., Choi, J. K., Yang, H., Lee, S., and Ryu, J. H.: Monitoring changes in suspended sediment concentration on the southwestern coast of Korea, Journal of Coastal Research, 70, 133-138, 2014.
Mishra, M., Acharyya, T., Santos, C. A. G., da Silva, R. M., Kar, D., Kamal, A. H. M., and Raulo, S.: Geo-ecological impact assessment of severe cyclonic storm Amphan on Sundarban mangrove forest using geospatial technology, Estuarine, Coastal and Shelf Science, 260, 107486, https://doi.org/10.1016/j.ecss.2021.107486, 2021a.
Mishra, M., Santos, C. A. G., da Silva, R. M., Rana, N. K., Kar, D., and Parida, N. R.: Monitoring vegetation loss and shoreline change due to tropical cyclone Fani using Landsat imageries in Balukhand-Konark Wildlife Sanctuary, India, Journal of Coastal Conservation, 25(6), 1-11, https://doi.org/10.1007/s11852-021-00840-5, 2021b.
Moon, I. J., Oh, I. S., Murty, T., and Youn, Y. H.: Causes of the unusual coastal flooding generated by Typhoon Winnie on the west coast of Korea, Natural Hazards, 29(3), 485-500, https://doi.org/10.1023/A:1024798718572, 2003.
Na, C. K.: Heavy metals in sediments and organisms from tidal flats along the Mokpo coastal area, Economic and Environmental Geology, 37(3), 335-345, 2004.
Nandi, G., Neogy, S., Roy, A. K., and Datta, D.: Immediate disturbances induced by tropical cyclone Fani on the coastal forest landscape of eastern India: A geospatial analysis, Remote Sensing Applications: Society and Environment, 20, 100407, https://doi.org/10.1016/j.rsase.2020.100407, 2020.
Nayak, S.: Use of satellite data in coastal mapping, Indian Cartographer, 22(147-157), 1, 2002.
NGII.: Digital elevation model, NGII (National Geographical Information Institute), the Ministry of Land, Infrastructure and Transport, Korea, 2018.
Parida, B. R., Behera, S. N., Oinam, B., Patel, N. R., and Sahoo, R. N.: Investigating the effects of episodic Super-cyclone 1999 and Phailin 2013 on hydro-meteorological parameters and agriculture: An application of remote sensing, Remote Sensing Applications: Society and Environment, 10, 128-137, https://doi.org/10.1016/j.rsase.2018.03.010, 2018.

Park, J. H., Yeo, D. E., Lee, K., Lee, H., Lee, S. W., Noh, S., ..., and Nam, S.: Rapid decay of slowly moving Typhoon Soulik (2018) due to interactions with the strongly stratified northern East China Sea, Geophysical Research Letters, 46(24), 14595-14603, https://doi.org/10.1029/2019GL086274, 2019.

Phiri, D., Simwanda, M., and Nyirenda, V.: Mapping the impacts of cyclone Idai in Mozambique using Sentinel-2 and OBIA approach, South African Geographical Journal, 103(2), 237-258, https://doi.org/10.1080/03736245.2020.1740104, 2021.

Rodgers, J. C., Murrah, A. W., and Cooke, W. H.: The impact of Hurricane Katrina on the coastal vegetation of the Weeks Bay Reserve, Alabama from NDVI data, Estuaries and Coasts, 32(3), 496-507, https://doi.org/10.1007/s12237-009-9138-z, 2009.

Rouse, J. W., Haas, J. R. H., Schell, J. A., and Deering, D. W.: Monitoring vegetation systems in the Great Plains with ERTS, In Proceedings of the 3rd ERTS Symposium, Washington, DC, USA, 1, 1974.

Ryang, W. H., Kang, S. I., and Cho, K. S.: Characteristics of Surface Topography and Sediments before and after the Typhoon Soulik in 2018, Macrotidal Coast of Gochang, Korea, In AGU Fall Meeting Abstracts, OS33B-02, 2021.

Sadik, M., Nakagawa, H., Rahman, M., Shaw, R., Kawaike, K., and Parvin, G. A.: Assessment of cyclone Aila recovery progress in Bangladesh: a comparison between rice and shrimp farming villages in Koyra, In Water, Flood Management and Water Security Under a Changing Climate, Springer, Cham, 109-124, 2020.

Sahoo, B. and Bhaskaran, P. K.: Multi-hazard risk assessment of coastal vulnerability from tropical cyclones–A GIS based approach for the Odisha coast, Journal of Environmental Management, 206, 1166-1178, https://doi.org/10.1016/j.jenvman.2017.10.075, 2018.

Santos, C. A. G., do Nascimento, T. V. M., Mishra, M., and da Silva, R. M.: Analysis of long- and short-term shoreline change dynamics: A study case of João Pessoa city in Brazil, Science of the Total Environment, 769, 144889, https://doi.org/10.1016/j.scitotenv.2020.144889, 2021.

Schneider, A.: Monitoring land cover change in urban and peri-urban areas using dense time stacks of Landsat satellite data and a data mining approach, Remote Sensing of Environment, 124, 689-704, https://doi.org/10.1016/j.rse.2012.06.006, 2012.

Shahzad, M. I., Meraj, M., Nazeer, M., Zia, I., Inam, A., Mehmood, K., and Zafar, H.: Empirical estimation of suspended solids concentration in the Indus Delta Region using

Landsat-7 ETM+ imagery, Journal of Environmental Management, 209, 254-261., https://doi.org/10.1016/j.jenvman.2017.12.070, 2018.

Shamsuzzoha, M., Noguchi, R., and Ahamed, T.: Damaged area assessment of cultivated agricultural lands affected by cyclone bulbul in coastal region of Bangladesh using Landsat 8 OLI and TIRS datasets, Remote Sensing Applications: Society and Environment, 23, 100523, https://doi.org/10.1016/j.rsase.2021.100523, 2021.

Sobrino, J. A., Jiménez-Muñoz, J. C., and Paolini, L.: Land surface temperature retrieval from LANDSAT TM 5, Remote Sensing of Environment, 90(4), 434-440, https://doi.org/10.1016/j.rse.2004.02.003, 2004.

Son, S., Kim, Y. H., Kwon, J. I., Kim, H. C., and Park, K. S.: Characterization of spatial and temporal variation of suspended sediments in the Yellow and East China Seas using satellite ocean color data, GIScience & Remote Sensing, 51(2), 212-226, https://doi.org/10.1080/15481603.2014.895580, 2014.

Song, W., Mu, X., Ruan, G., Gao, Z., Li, L., and Yan, G.: Estimating fractional vegetation cover and the vegetation index of bare soil and highly dense vegetation with a physically based method, International journal of applied earth observation and geoinformation, 58, 168-176, https://doi.org/10.1016/j.jag.2017.01.015, 2017.

Souza, A. J., Dickey, T. D., and Chang, G. C.: Modeling water column structure and suspended particulate matter on the Middle Atlantic continental shelf during the passages of Hurricanes Edouard and Hortense, Journal of Marine Research, 59(6), 1021-1045, https://doi.org/10.1357/00222400160497751, 2001.

Story, M. and Congalton, R. G.: Accuracy assessment: a user's perspective, Photogrammetric Engineering and Remote Rensing, 52(3), 397-399, 1986.

Tang, R., Shen, F., Ge, J., Yang, S., and Gao, W.: Investigating typhoon impact on SSC through hourly satellite and real-time field observations: A case study of the Yangtze Estuary, Continental Shelf Research, 224, 104475, https://doi.org/10.1016/j.csr.2021.104475, 2021.

Thieler, E. R., Himmelstoss, E. A., Zichichi, J. L., and Ergul, A.: The Digital Shoreline Analysis System (DSAS) version 4.0-an ArcGIS extension for calculating shoreline change (No. 2008-1278), US Geological Survey, 2009.

Tian, Y., Mingming, J., Zongming, W., Dehua, M., Baojia, D., and Chao, W.: Monitoring invasion process of Spartina alterniflora by seasonal Sentinel-2 imagery and an object-based random forest classification, Remote Sensing, 12(9), 1383, https://doi.org/

10.3390/rs12091383, 2020.

Tsai, C. H., Tzang, S. Y., Hsiao, S. S., Cheng, C. C., and Li, H. W.: Coastal structure failures and coastal waves on the north coast of Taiwan due to typhoon Herb, Journal of Coastal Research, 22(2), 393-405, 2006.

Tsai, Y. L. S.: Monitoring 23-year of shoreline changes of the Zengwun Estuary in Southern Taiwan using time-series Landsat data and edge detection techniques, Science of The Total Environment, 156310, https://doi.org/10.1016/j.scitotenv.2022.156310, 2022.

Wang, W., Qu, J. J., Hao, X., Liu, Y., and Stanturf, J. A.: Post-hurricane forest damage assessment using satellite remote sensing, Agricultural and forest meteorology, 150(1), 122-132, https://doi.org/10.1016/j.agrformet.2009.09.009, 2010.

Wang, T., Liu, G., Gao, L., Zhu, L., Fu, Q., and Li, D.: Biological and nutrient responses to a typhoon in the Yangtze Estuary and the adjacent sea, Journal of Coastal Research, 32(2), 323-332, 2016.

Wang, M. and Xu, H.: Remote sensing-based assessment of vegetation damage by a strong typhoon (Meranti) in Xiamen Island, China, Natural Hazards, 93(3), 1231-1249, https://doi.org/10.1007/s11069-018-3351-7, 2018.

Wang, S., Mu, L., Qi, M., Yu, Z., Yao, Z., and Zhao, E.: Quantitative risk assessment of storm surge using GIS techniques and open data: A case study of Daya Bay Zone, China, Journal of Environmental Management, 289, 112514, https://doi.org/10.1016/j.jenvman.2021.112514, 2021.

WMO (World Meteorological ~~Organisation~~Organization): Tropical cyclones~~.~~, Retrieved May 06, 2020 from https://public.wmo.int/en/our-mandate/focus-areas/natural-hazards-and-disaster-risk-reduction/tropical-cyclones , 2020.

Wong, M. M. F., Fung, J. C. H., and Yeung, P. P. S.: High-resolution calculation of the urban vegetation fraction in the Pearl River Delta from the Sentinel-2 NDVI for urban climate model parameterization, Geoscience Letters, 6(1), 1-10, https://doi.org/10.1186/s40562-019-0132-4, 2019.

Xu, S., Zhu, X., Helmer, E. H., Tan, X., Tian, J., and Chen, X.: The damage of urban vegetation from super typhoon is associated with landscape factors: Evidence from Sentinel-2 imagery, International Journal of Applied Earth Observation and Geoinformation, 104, 102536, https://doi.org/10.1016/j.jag.2021.102536, 2021.

Yang, Q., Qin, Z., Li, W., and Xu, B.: Temporal and spatial variations of vegetation cover in Hulun Buir grassland of Inner Mongolia, China, Arid Land Research and Management, 26(4), 328-343, https://doi.org/10.1080/15324982.2012.709215, 2012.

Yang, Y., Erskine, P. D., Lechner, A. M., Mulligan, D., Zhang, S., and Wang, Z.: Detecting the dynamics of vegetation disturbance and recovery in surface mining area via Landsat imagery and LandTrendr algorithm, Journal of Cleaner Production, 178, 353-362, https://doi.org/10.1016/j.jclepro.2018.01.050, 2018.

Yin, J., Yin, Z., and Xu, S.: Composite risk assessment of typhoon-induced disaster for China's coastal area, Natural hazards, 69(3), 1423-1434, https://doi.org/10.1007/s11069-013-0755-2, 2013.

Yoon, W. S., Yoon, S. H., Moon, J. H., and Hong, J. S.: Topographic Variability during Typhoon Events in Udo Rhodoliths Beach, Jeju Island, South Korea, Ocean and Polar Research, 43(4), 307-320., 2021.

Yu, J. J., Kim, D., and Yoon, J.: A Study on the Short-term Morphological Beach Changes of Pado-ri Using UAS-based DEM: Focusing on before and after Typhoon Soulik, Journal of the Association of Korean Geographers, 7(3), 303-317, 2018.

Yum, S. G., Wei, H. H., and Jang, S. H.: Estimation of the non-exceedance probability of extreme storm surges in South Korea using tidal-gauge data, Natural Hazards and Earth System Sciences, 21(8), 2611-2631, https://doi.org/10.5194/nhess-21-2611-2021, 2021.

Zhang, X., Wang, Y., Jiang, H., and Wang, X.: Remote-sensing assessment of forest damage by Typhoon Saomai and its related factors at landscape scale, International Journal of Remote Sensing, 34(21), 7874-7886, https://doi.org/10.1080/01431161.2013.827344, 2013.

Zhang, J., Zhang, Z., Chen, J., Chen, H., Jin, J., Han, J., ... and Wei, G.: Estimating soil salinity with different fractional vegetation cover using remote sensing, Land Degradation & Development, 32(2), 597-612, https://doi.org/10.1002/ldr.3737, 2021.

Zhang, Y., Sun, Y., Hu, Z., Bian, S., Xiong, C., Liu, J., ... , and Zhang, W.: Increase in Suspended Sediment Contents by a Storm Surge in Southern Bohai Sea, China, Mathematical Problems in Engineering, 2022, https://doi.org/10.1155/2022/9585386, 2022.